ABSTRACT

(Physics)

FINE STRUCTURE OF ANALOG STATES IN ^{55}Co, ^{57}Co, AND ^{59}Co

by

Daniel Peter Lindstrom

Department of Physics
Duke University

Date: _____

Approved:

_____
E. G. Bilpuch, Supervisor

_____

_____

_____

_____

An abstract of a dissertation submitted in partial fulfillment of the requirements for the degree of Doctor of Philosophy in the Department of Physics in the Graduate School of Arts and Sciences of Duke University

1970

FINE STRUCTURE OF ANALOG STATES

IN ^{55}Co, ^{57}Co, AND ^{59}Co

by

Daniel Peter Lindstrom

Differential cross sections for ^{54}Fe(p,p), ^{56}Fe(p,p), and ^{58}Fe(p,p) were measured at laboratory angles of 160°, 135°, 120°, and 90° for proton energies of between 1.8 and 3.3 MeV. These data were taken using the high resolution electrostatic analyzer-homogenizer system in the 3 MV Van de Graaff laboratory, which is part of the Triangle Universities Nuclear Laboratory at Duke University. Thin targets of enriched isotopes were used, and the observed energy resolution was 300-400 eV.

Analogs of four excited states of ^{55}Fe were identified in the ^{54}Fe(p,p) experiment. The analog of the seventh excited state of ^{57}Fe was identified and two higher excited states tentatively identified in the ^{56}Fe(p,p) experiment. The analogs of the ground state and first excited state of ^{59}Fe were observed in the ^{58}Fe(p,p) experiment. Only the latter

two analogs were significantly fragmented, the other analogs appearing as one or two levels. Analysis of the data using single-level or multi-level R-matrix codes yielded resonance parameters, which were used to calculate spectroscopic factors for each analog. The single particle widths used in extracting spectroscopic factors were calculated using three different methods. Comparison with spectroscopic factors from (d,p) experiments reveals discrepancies in some cases and agreement in others.

Coulomb energy differences between the analogs and their parent states were extracted, yielding results consistent with those of other experiments.

Resonances not associated with analog states yielded information about proton strength functions and level spacings. For a given spin and parity, considerable variation of strength functions was noted between the three isotopes investigated.

ACKNOWLEDGMENTS

I would like to thank my advisor, Professor E. G. Bilpuch, for his interest and patient guidance over the past few years, which made this research possible. Special thanks go to Professor G. E. Mitchell for his continuing interest and invaluable discussions during the course of this experiment. The support of Professor H. W. Newson was greatly appreciated. Credit for sparking my interest in this field of research and helping me throughout its early stages goes to Dr. G. A. Keyworth.

Dr. J. C. Browne and Dr. J. D. Moses have rendered assistance to me in innumerable ways, and for their help I am deeply grateful. The help of N. H. Prochnow and W. M. Wilson in taking some of the data was appreciated.

The figures in this dissertation were expertly drawn by Mrs. Joseph Bailey. The assistance of Mr. S. E. Edwards and Mr. R. L. Rummel in maintaining the equipment is gratefully acknowledged.

This work was supported in part by the United States

Atomic Energy Commission. Data Analysis was performed at the Triangle Universities Computation Center, which is supported in part by the National Science Foundation.

D. P. L.

CONTENTS

LIST OF FIGURES

LIST OF TABLES

FINE STRUCTURE OF ANALOG STATES IN ^{55}Co, ^{57}Co, AND ^{59}Co

Chapter I

INTRODUCTION

In recent years, the study of isobaric analog states has become established as an extremely significant and productive subfield of nuclear physics. Experimentalists using a variety of experimental techniques and theorists using differing theoretical approaches have very rapidly developed this highly active field. A brief historical survey seems appropriate, to recapitulate the growth and development of interest in isobaric analog states.

Soon after the discovery of the neutron in 1932, the similar properties of the neutron and proton led Heisenberg to propose the concept of isospin. In this formalism the neutron and proton are treated as being one of two possible isospin states of a more general entity, the nucleon. The analogy with intrinsic spin led to the adoption of Pauli's spinor algebra. Thus the isospin quantum number, T, was introduced. By convention the component $T_z = +1/2$ corresponds to the neutron and $T_z = -1/2$ corresponds to the proton,

so that a nucleus has a total isospin projection of T_z = (N - Z)/2. In 1937 Wigner proposed that the total isospin should be a good quantum number for nuclei in which the Coulomb interaction was small compared to the nuclear interaction. Early work involving isospin was confined to light nuclei for which Coulomb forces were small.

More recently, a study of (p,n) reactions in heavier nuclei ($48 \leq A \leq 93$) by Anderson, et al. (1962) suggested that isospin is also a reasonably good quantum number in heavy nuclei. They found that a strong neutron peak appeared at a neutron energy equal to the difference between the incident proton energy and the Coulomb energy of a proton in the residual nucleus. This strong neutron group was interpreted as the product of a charge exchange reaction which left the residual nucleus in a highly excited state whose quantum numbers differed from the ground state of the target nucleus only in having a T_z differing by one unit. The state of the residual nucleus was termed an "analog state", while the corresponding state of the target nucleus was called the "parent" state.

These pioneering studies of analog states through (p,n) charge exchange reactions were followed by the discovery by Fox, et al. (1964) of analog states in the proton plus target system (p + C) of even-even nuclei. A proton

($T_z = -1/2$) impinging on a target with isospin $T = T_o$ yields a compound system (p + C) containing both states of $T = T_z = T_< = T_o - 1/2$ and $T = T_> = T_o + 1/2$. The latter states are analogs of $T_o + 1/2$ states of the neutron plus target system (n + C). These analog states have the same quantum numbers as the corresponding parent states, but the energy is shifted by the Coulomb energy of the additional proton, minus the neutron-proton mass difference.

Although analog states in the compound system first appeared as single resonances, Richard, et al. (1964) performed an experiment with improved proton energy resolution which suggested that the analog state might actually be composed of a number of resonances. This was confirmed by Keyworth, et al. (1966) who performed the $^{40}A(p,p)$ experiment using very high energy resolution and a thin gas target in a cryogenically pumped windowless target chamber. This experiment revealed clearly that the analog state comprised an ensemble of "fine structure" states. This fine structure apparently arises from isospin mixing of the analog state with the normal $T_<$ states of the same spin and parity.

Additional high resolution studies of analog states were clearly of great interest. Unfortunately, few gases have characteristics suitable for use in the cryogenic target chamber. Therefore, efforts were made to extend the methods

of high resolution proton scattering to solid targets. Preliminary experiments using thin calcium targets were performed in this laboratory (Browne, et al., 1968; Wilhjelm, et al., 1969). After these promising preliminary results, a target chamber suitable for charged particle scattering experiments using solid targets was built, using many of the components of the cryogenic target chamber. A systematic investigation of analog states in a large number of medium weight ($40 \lesssim A \lesssim 70$) isotopes was begun.

Three even-even iron isotopes were available commercially in enriched form: ^{54}Fe, ^{56}Fe, and ^{58}Fe. Calculations indicated that several $\ell = 1$ analog states in each compound system should fall within the energy range available on the 3 MV Van de Graaff accelerator. Level densities of $T_<$ background states were low enough and proton widths large enough that most of these analogs were expected to be both observable and amenable to analysis.

Differential cross sections were measured for $^{54}Fe(p,p)$, $^{56}Fe(p,p)$, and $^{58}Fe(p,p)$ over an energy range of 1.8 to 3.3 MeV at laboratory angles of 160°, 135°, 120° (or 105°), and 90°. Inelastic protons from the $^{56}Fe(p,p')^{56}Fe^{*}$ reaction were detected, but the large background from the carbon backings made analysis of these data very difficult. The partial widths for inelastic scattering were small enough

to be neglected in analyzing most of the elastic scattering data, with several exceptions noted in Chapter V. Analysis of the elastic scattering data on these three iron isotopes yielded spectroscopic factors, Coulomb energy differences, and proton strength functions.

A survey of relevant theoretical topics appears in the following chapter. Chapter III contains a description of the experimental equipment and target preparation procedures. Data analysis methods are described in Chapter IV, which includes plots of the elastic scattering data taken at 160°. Discussions of the analog states observed, spectroscopic factors, Coulomb displacement energies, and proton strength functions appear in Chapter V.

Chapter II

THEORY

The study of analog states with high resolution elastic proton scattering involves both the R-matrix theory of nuclear reactions and the theories of analog states. The R-matrix theory has become rather firmly established through successful application over a period of many years. Several theories of analog states have been proposed in recent years and are currently being refined to cope with new experimental results. Only a brief outline of the directly relevant features of these theories will be included here.

A. R - Matrix Theory

Protons incident upon a target nucleus can lead to the formation of compound nuclear states symbolized by $|pC\rangle$, for proton + core. These states are characterized by the total angular momentum J, parity π, and widths for various

modes of decay. Wigner and Eisenbud (1947) developed the R-matrix theory of nuclear reactions, which enables these resonance parameters to be extracted from various types of scattering data. A comprehensive review article of R-matrix theory has been written by Lane and Thomas (1958).

One assumption of the R-matrix approach is that only two-body reactions are considered. Thus the compound nuclear state decays into two parts α_1 and α_2. Coupling these wave functions yields sets of quantum numbers which characterize the possible "channels" through which decay may proceed. Associated with these channels are radii (a_c) beyond which the two fragments are assumed to experience no nuclear forces. This amounts to partitioning space into an "internal" region and an "external" region. A complete set of compound nuclear states which satisfy the nonrelativistic Schrödinger equation are defined in the internal region and join the external wave functions, subject to boundary conditions at the channel radius. A matrix formalism is introduced and the scattering process is described in terms of the R matrix, which contains the internal interactions, and the L and Ω matrices which contain the external interactions.

The R-matrix theory is very general in that a wide range of nuclear reactions may be treated without introducing detailed nuclear models. Cross sections for overlapping

resonances as well as isolated resonances may be derived from the theory, and computer codes for both single-level and multi-level cases were utilized in the present analysis. The formula used in calculating single-level cross sections is given by Keyworth (1968) and the more complicated multi-level formula is given by Sellin (1968).

B. Analog States

The addition of a proton ($T_z = -1/2$) to a target of isospin T_o leads to the formation of two possible isospin states, $|T_o+1/2,\ T_o-1/2\rangle = |T_>\rangle$ and $|T_o-1/2,\ T_o-1/2\rangle = |T_<\rangle$. The compound system formed by the addition of a neutron to a target may be represented by $|nC\rangle = |T_o+1/2,\ T_o+1/2\rangle$. It is convenient to define an isobaric spin lowering operator, analogous to the usual angular momentum lowering operator, which obeys

$$T^- |T,T_z\rangle = \sqrt{(T+T_z)(T-T_z+1)}\ |T,T_z-1\rangle. \qquad (1)$$

Applying T^- to the $|nC\rangle$ states, one obtains

$$T^- |nC\rangle = (2T_o+1)^{\frac{1}{2}} |T_o+1/2, T_o-1/2\rangle = (2T_o+1)^{\frac{1}{2}} |T_>\rangle. \qquad (2)$$

Thus the analog states in the proton + target (p + C) system are obtained by applying the T^- operator to states in the parent neutron + target (n + C) system.

Figure 1 shows the energy relationship between the parent and analog states. The center-of-mass proton energy required to populate the analog of the ground state of the $|nC\rangle$ system is

$$E_p^{CM} = \Delta E_C - B_n \qquad (3)$$

where ΔE_C is the Coulomb energy of the added proton, and B_n is the binding energy of the last neutron in the $|nC\rangle$ system. Analogs of excited states are of course observable at higher proton energies.

Several theories have been proposed to explain the details of analog states. Although these theories are quite different formally, they yield similar results. The first systematic treatment of analog states was given by Robson (1965). He assumes that within a certain radius, a_c, isospin may be a good quantum number even though Coulomb forces strongly mix $T_<$ and $T_>$ states outside this radius. This partition of space is similar to the spatial division assumed in R-matrix theory. Robson utilized the R-matrix framework in his theory. He assumed a potential of the form $V_C(r) + U_O(r) + U_1(r)(\vec{t}\cdot\vec{T})$, where $V_C(r)$ is the Coulomb potential, $U_O(r)$ is the normal optical potential, and $U_1(r)$ $(\vec{t}\cdot\vec{T})$ is the isospin-dependent part of the optical potential. This potential had been successfully used by Lane (1962) to treat (p,n) charge exchange analog state experiments. This

Figure 1. Diagram of the Relationships Between the Analog State and the Parent State.

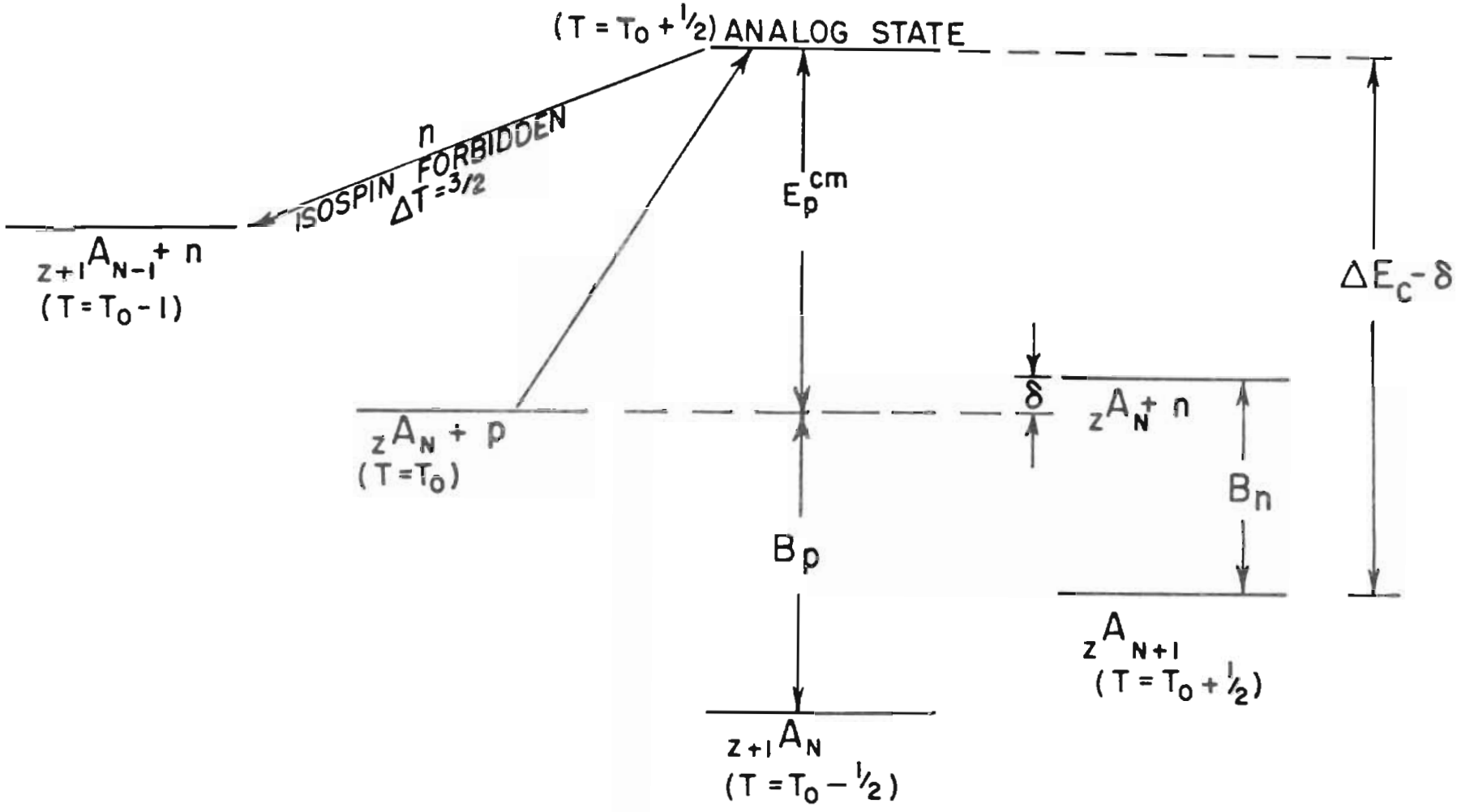

δ = neutron - proton mass difference

potential results in two coupled equations. These can be diagonalized by introducing the basis functions $\chi_>$ and $\chi_<$, which are eigenfunctions of $T_>$ and $T_<$, respectively. The degree of coupling between $\chi_>$ and $\chi_<$ is found to depend on $(\Delta E_c - V_c)$, which is generally much smaller in the internal region than in the external region.

In agreement with experimental results, Robson's theory predicted that the widths of $T_<$ states having the same spin and parity as the analog would be increased by the presence of a nearby analog state. Furthermore, an effect of external mixing was an asymmetric enhancement, such that the widths of $T_<$ states below the analog are enhanced more than those above the analog. This asymmetry has been observed in a number of fine-structure experiments.

One quantity of interest is the "spectroscopic factor", which is the fraction of a particular state that is described as a single particle plus an inert core. The spectroscopic factor for parent neutron states is usually derived from (d,p) stripping measurements. In the particle-hole representation of an analog state shown in fig. 2, there are $(N - Z) = 2T_z$ neutrons available to form 2-particle, 1-hole states. Since only the single particle state is excited in proton elastic scattering, it is natural to define the spectroscopic factor for the analog state as follows:

$$S_{pp} = (2T_o + 1)\Gamma_p/\Gamma_{sp}, \qquad (4)$$

where Γ_p is the observed proton elastic scattering width of the analog state and Γ_{sp} is the calculated proton single particle width. The procedure used to calculate the single particle width is described in Chapter V.

A sum rule must be applied to the reduced widths of the fine structure states in order to extract Γ_p. The relation of the reduced proton width, γ_p^2, to the observed width is given by

$$\gamma_p^2 = \Gamma_p/2P_p. \qquad (5)$$

The penetration factor P_p is related to the probability that a proton will penetrate the Coulomb and centrifugal barriers. To calculate γ_p^2, Robson (1966) gives the following sum rule:

$$\gamma_p^2 = \sum_{\mu} \gamma_{\mu p}^2 - \sum_{\nu} \gamma_{\nu p}^2 \qquad (6)$$

where the $\gamma_{\mu p}^2$ are the reduced widths of the fine structure states comprising the analog, and the $\gamma_{\nu p}^2$ are the reduced widths of the states before isospin mixing is introduced. In favorable cases, the latter sum can be estimated by determining the average reduced width of $T_<$ states (having the same spin as the analog) away from the analog state.

Figure 2. Particle - Hole Picture of the Analog State

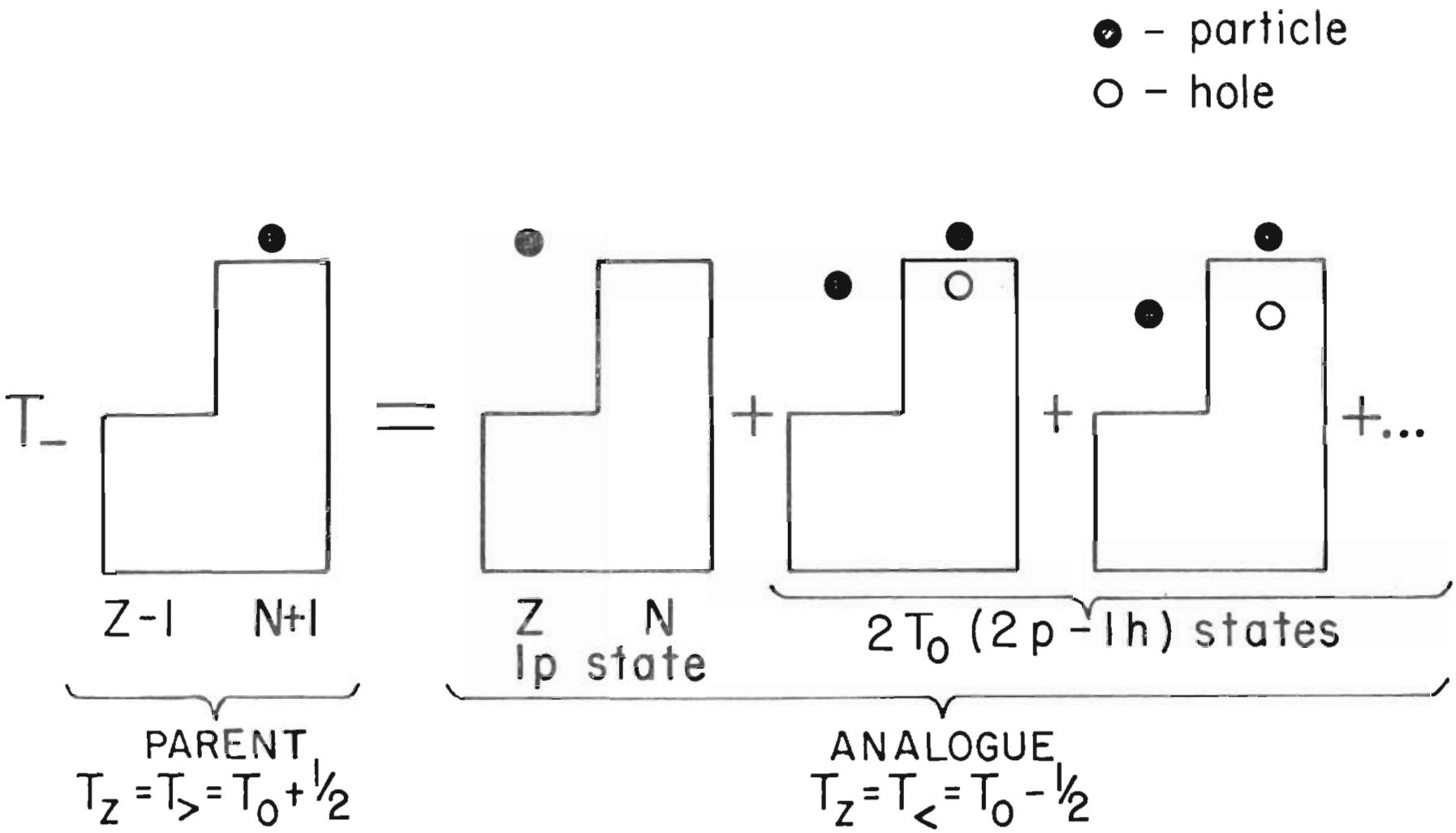
● – particle
○ – hole
T–
=
+
+
+...
Z-1 N+1
Z N
1p state
2 T0 (2p-1h) states
PARENT
Tz = T> = T0 + ½
ANALOGUE
Tz = T< = T0 - ½

Chapter III

EXPERIMENTAL EQUIPMENT AND PROCEDURE

The data presented here were taken using the 3 MV Van de Graaff accelerator and the associated high resolution equipment described in detail by Toller (1954) and by Parks, et al. (1958). Several refinements of this equipment are discussed in a dissertation by Seibel (1968). The main features of the energy stabilization system may be seen in the laboratory floor plan of fig. 3. The analyzing magnet deflects the proton beam 25° into the target chamber and the HH^{+} beam 17° into the one-meter cylindrical electrostatic analyzer. A difference signal derived from the image slits of the analyzer is amplified and applied to the target rod, cancelling out much of the energy fluctuation of the proton beam. Part of this correction signal is applied to the outer plate of the analyzer to keep the HH^{+} beam centered and to close the feedback loop. An advantage of this system is that only the molecular beam is used for energy stabilization, and the proton beam intensity is unimpaired.

Figure 3. Floor Plan of the 3 MV Laboratory High Resolution System.

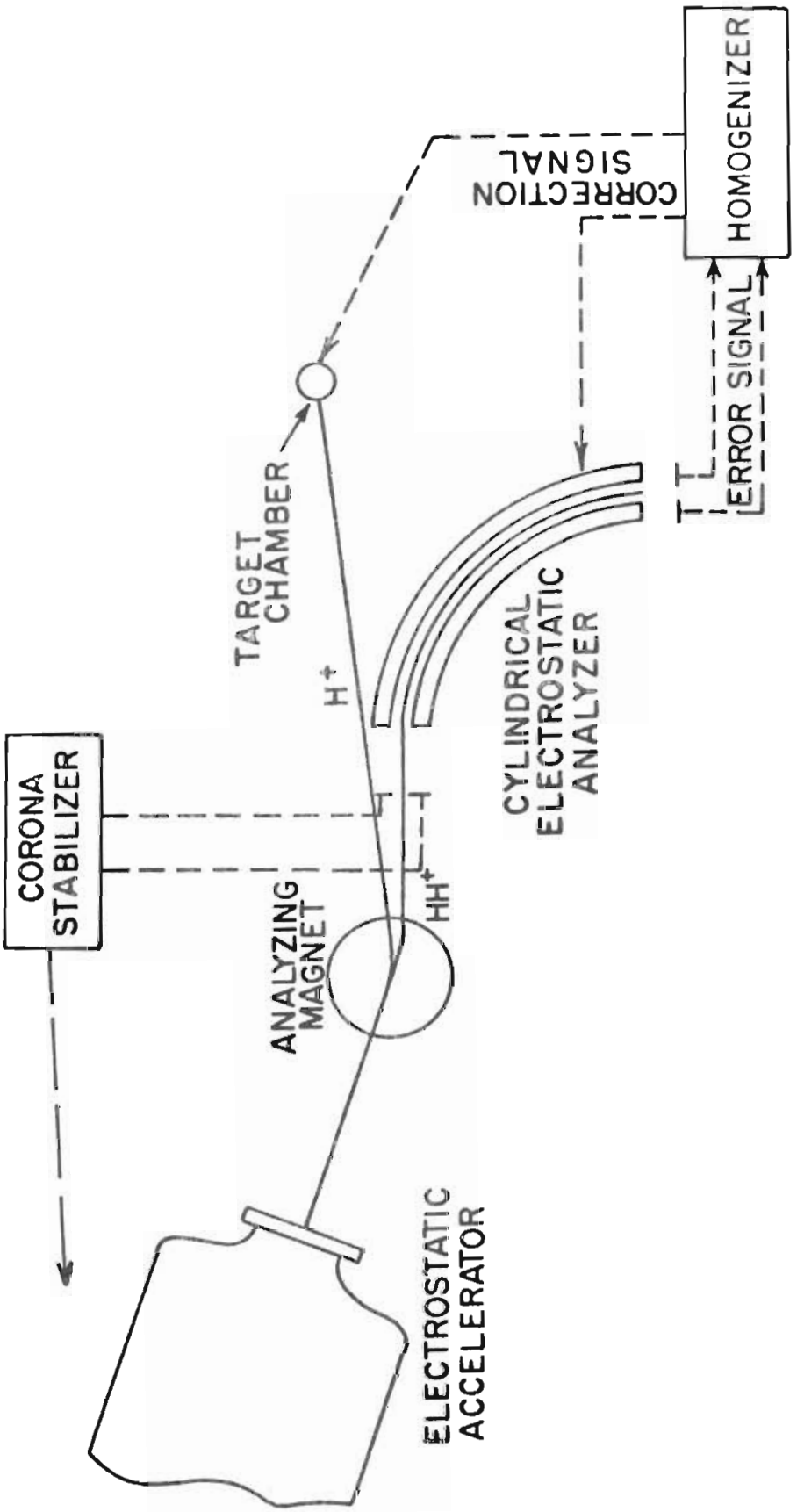
HOMOGENIZER
CORRECTION SIGNAL
ERROR SIGNAL
TARGET CHAMBER
H+
CYLINDRICAL ELECTROSTATIC ANALYZER
CORONA STABILIZER
ANALYZING MAGNET
HH+
ELECTROSTATIC ACCELERATOR

Although proton beams on the order of 100 μA are readily attainable with this system, the intensity was limited to 5 - 10 μA by the ability of the targets to withstand heat without breaking.

A null-type digital voltmeter monitors the potential across part of a precision resistor stack connected to the inner plate of the analyzer. A differential output from this voltmeter is amplified by the proper factor and applied to the outer analyzer plate. In this way, energy variations due to drift in the analyzer high voltage power supply are removed. The calibration is such that the digital voltmeter gives the proton energy directly. This calibration was checked periodically by measuring the $^{7}Li(p,n)^{7}Be$ threshold.

A. Detectors and Electronics

A block diagram of the electronics used is shown in fig. 4. Data were taken at four angles simultaneously, so four detectors, amplifiers, single channel analyzers, and scalers were used. The silicon surface barrier detectors used had a depletion depth of 300-500 microns. The multi-channel analyzer and pulser were used for setting the "window" of the single channel analyzer on the elastic iron peak.

Figure 4. Block Diagram of the Charged Particle Counting System.

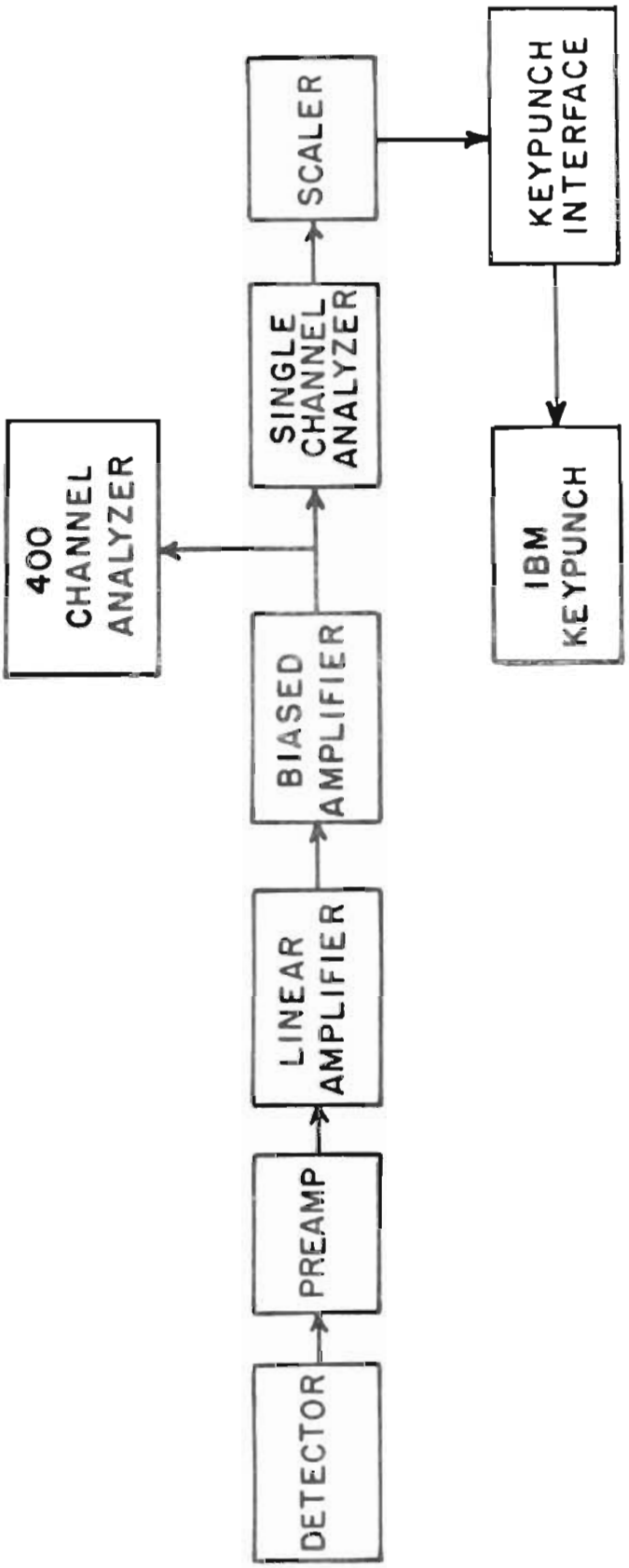
DETECTOR
PREAMP
LINEAR AMPLIFIER
BIASED AMPLIFIER
400 CHANNEL ANALYZER
SINGLE CHANNEL ANALYZER
SCALER
KEYPUNCH INTERFACE
IBM KEYPUNCH

Data were read out onto punched cards using a digital readout system which is described in detail in the appendix. A beam current integrator was used to establish the accumulation time at each energy point; counting times averaged about fifteen seconds per data point. An integrated charge of 60-120 μC was sufficient to maintain statistics of 1-2% in the off-resonance Coulomb scattering. The yield was monitored by reading out a digital timer along with the scalers.

The target chamber had provisions for six detectors at laboratory angles of 160°, 150°, 135°, 120°, 105°, and 90°. The vacuum in the chamber was maintained at about 5×10^{-7} torr, thus reducing buildup of contaminants on the target to an extremely low level. The target rod fits into an airlock which can be pumped out separately, so that targets may be inserted without disturbing the vacuum of the target chamber. A more detailed description of the target chamber appears in a dissertation by Browne (1969).

B. Target Preparation

Targets were prepared by vacuum evaporation onto 10 or 20 $\mu g/cm^2$ carbon foils. The samples of ^{54}Fe and ^{56}Fe were of 98% and 99.9% purity, respectively, but the ^{58}Fe

sample contained only 82% ^{58}Fe and about 16% ^{56}Fe. An additional background term was subtracted from the $^{58}Fe(p,p)$ data to compensate for the impurity. All isotopes were obtained from Oak Ridge in ferric oxide form. Evaporation proved to be difficult, since the iron readily formed alloys with any evaporation boat that was tried. In an effort to prevent the iron from alloying with the boat, aluminum oxide coated boats were tried. The oxide layer was penetrated by the iron at a temperature well below that required for evaporation. An attempt was also made to use a boron nitride crucible with an electron gun type heater, but nonuniform heating caused the iron to spatter out of the crucible. It was finally decided to use a tungsten boat, in spite of the fact that iron readily alloys with tungsten.

The typical spectrum of fig. 5 shows that an appreciable amount of tungsten is deposited on the target. Targets were found to contain about half as many tungsten atoms as iron atoms. By carefully setting the window of the single channel analyzer, the iron peak was separable from the tungsten peak, so the only effects of the tungsten were a slight degradation of energy resolution and an increase in background due to the tail of the tungsten peak. Neither of these effects was found to be particularly troublesome. Target thicknesses were calculated from off-resonance Coulomb scattering. Targets

of 1.5 to 2.5 $\mu g/cm^2$ iron thickness were used in these experiments, yielding a total energy spread of 300 to 400 eV.

Figure 5. Sample Spectrum in the ^{54}Fe(p,p) Experiment.

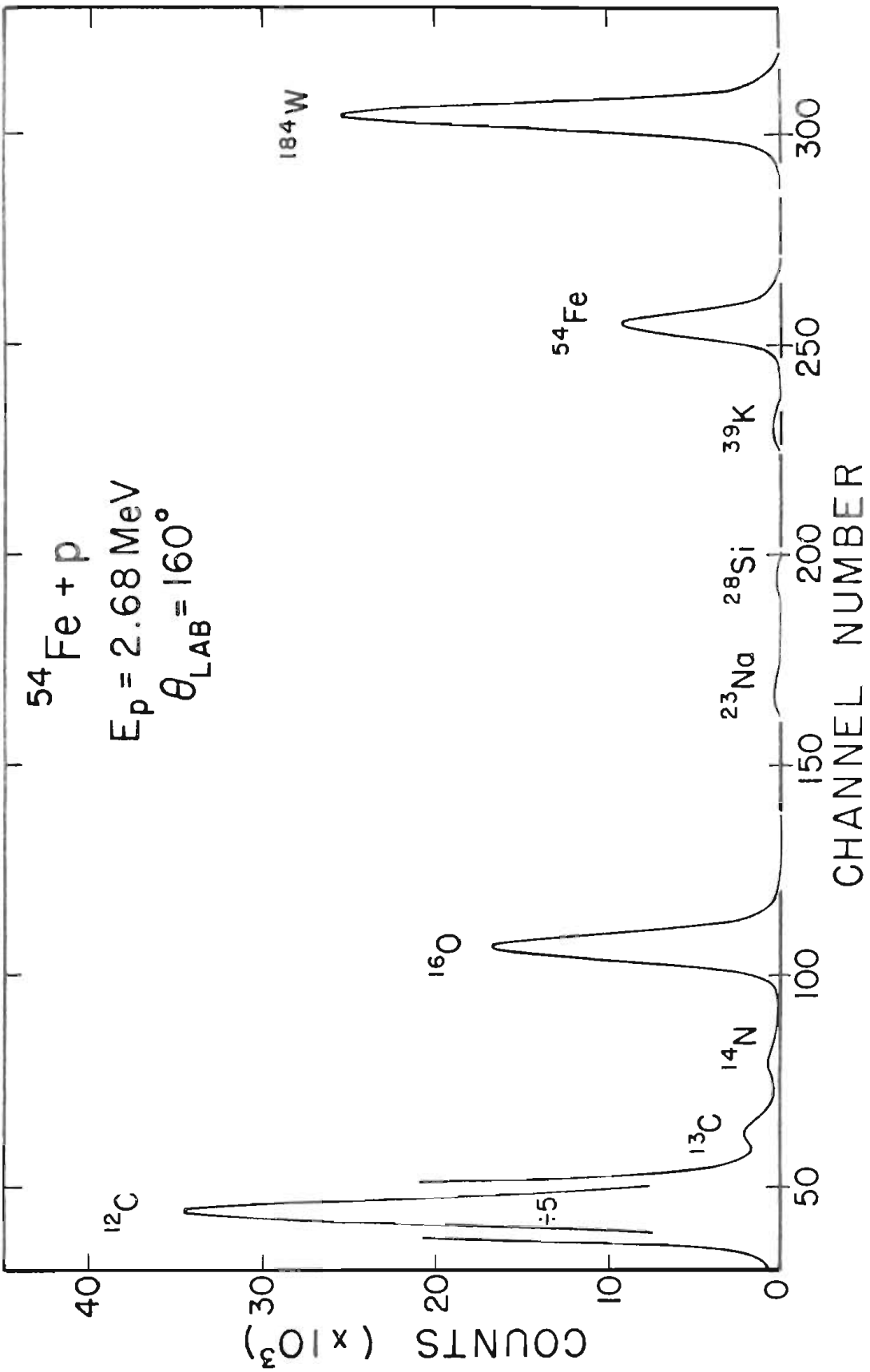
$^{54}Fe + p$
$E_p = 2.68$ MeV
$\theta_{LAB} = 160°$
^{12}C
÷5
^{13}C
^{14}N
^{16}O
^{23}Na
^{28}Si
^{39}K
^{54}Fe
^{184}W
COUNTS (x 10^3)
CHANNEL NUMBER
0
10
20
30
40
50
100
150
200
250
300

Chapter IV

ANALYSIS

Data were analyzed to extract resonance parameters for all resonances observed below a certain upper energy limit. In the $^{58}Fe(p,p)$ experiment, the density of $T_<$ states becomes so high that the data are very difficult to analyze above 2.7 MeV. Since the level density is somewhat lower for $^{56}Fe(p,p)$, the analysis was completed to 3.16 MeV. All resonances observed in the $^{54}Fe(p,p)$ experiment were analyzed.

Resonances which were sufficiently well separated were analyzed using a single-level Breit-Wigner code (Keyworth, 1968). This code uses an approximate linear regression technique to search over the resonant energy E_o, the total width Γ, the ratio Γ_p/Γ, and the resolution width Δ. Hard sphere scattering is included in this code, but since the proton energy was only about 40% of the Coulomb barrier height, this contribution to the cross section is small. After a consistent value for the resolution width was found, this parameter was held fixed for a given energy region.

The resolution function, which is approximated by a Gaussian shape, produced the best fits when the resolution width was 300-400 eV.

Either small penetrabilities or unfavorable kinematics eliminated all exit channels except the elastic channel for most of the energy range used. Inelastic protons were observed in ^{56}Fe + p, but only two resonances had $\Gamma_{p'}$ which was a significant fraction of Γ_p. This case is discussed more fully in the next chapter. The (p,n) channel opens at 3.15 MeV in ^{58}Fe, but the (p,p) data were not analyzed in this energy region, due to the high level density. The remainder of the data were fitted with Γ_p/Γ set to unity.

Background corrections were necessitated by two factors. A tungsten peak from the evaporation boat, while separable from the iron peak, left a low energy tail which added to the background under the iron peak. This background was estimated from multichannel analyzer spectra taken during each run. For ^{58}Fe targets, another background contribution was due to an 18% isotopic impurity in the sample.

Where resonances were not well separated, a multi-level, multi-channel R-matrix code was used (Sellin, 1968). No search routine was incorporated in this code, so the resonance parameters were changed manually until the best fit was obtained. The width of the Gaussian resolution

function was found by using the single-level search code on a nearby resonance. A typical multi-level fit is shown in fig. 6. Tables 1, 2, and 3 show the resonance parameters extracted from the $^{54}Fe(p,p)$, $^{56}Fe(p,p)$, and $^{58}Fe(p,p)$ data, respectively.

The energy calibration of the Van de Graaff accelerator was checked at the end of the experiment by measuring the $^{7}Li(p,n)$ threshold. Slow energy drifts were detected, probably due to temperature changes altering the geometry of the cylindrical electrostatic analyzer plates. This source of error was minimized by overlapping runs, but an estimated absolute energy error of $\pm$ 3 keV seems appropriate. The relative error between two nearby levels should be much less--on the order of 100 eV. For resonances of less than 30 eV observed width, the characteristic shapes of $1/2^-$ and $3/2^-$ resonances are similar, and these J assignments are uncertain. The same ambiguity is encountered with weak $3/2^+$ and $5/2^+$ resonances. This uncertainty is indicated by parentheses in tables 1, 2, and 3. Reduced widths were calculated from eq. (5). The proton penetrability (P_p) was calculated with Coulomb wave functions generated by the subroutine EXTFN (Gursky).

Figure 6. Multi-level Fit to a Portion of the $^{54}Fe(p,p)$ Data. The level at 2.751 MeV is the analog of the 3.029 MeV level in ^{55}Fe.

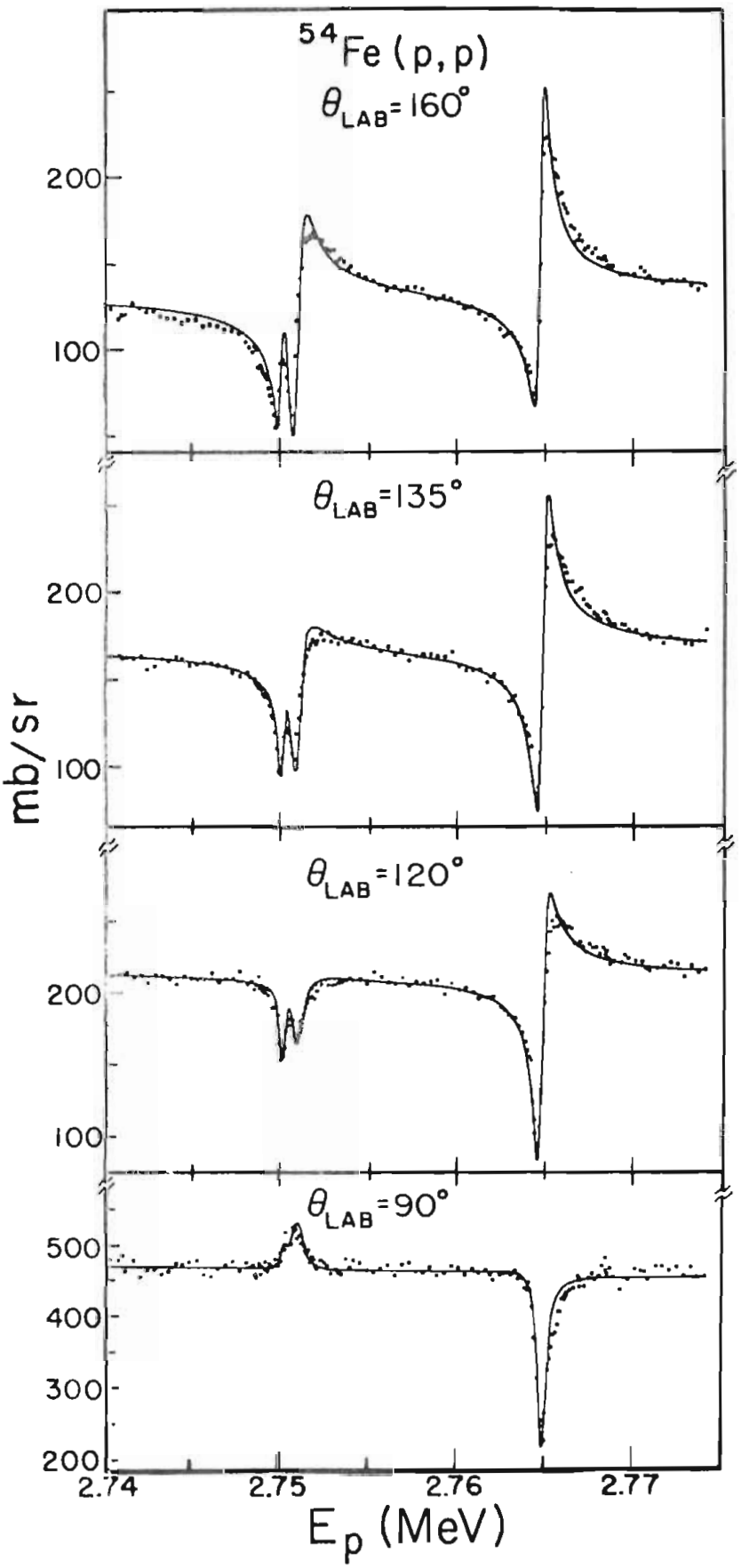
^{54}Fe (p, p)
θ_{LAB}= 160°
θ_{LAB}=135°
θ_{LAB}=120°
θ_{LAB}=90°
mb/sr
200
100
500
400
300
2.74
2.75
2.76
2.77
E_p (MeV)

A. $^{54}Fe(p,p)$

The level diagrams of fig. 7 show the energy levels of ^{55}Co and ^{55}Fe, with the latter shifted by $\Delta E_c - \delta$, where δ is the neutron-proton mass difference. The four $\ell = 1$ analog states in ^{55}Co observed in the present experiment are shown. Excitation energies, spectroscopic factors, and ℓ-values for ^{55}Fe are from Nuclear Data Sheets. The (d,p) spectroscopic factors represent averages of the results of Fulmer and McCarthy (1963), and those of Maxwell and Parkinson (1964). Since the ratio of the former to the latter values was as large as 2.7, agreement can hardly be expected between the average of these (d,p) results and spectroscopic factors obtained from the present experiment.

Figure 8 displays the $^{54}Fe(p,p)$ differential cross-section at 160°, over the energy range of 1.75 to 3.30 MeV. The solid line through the data is merely a visual aid, not a fit to the data. Notable is the wide spacing between resonances and the predominance of $1/2^-$ and strong $5/2^+$ levels. Level spacings were calculated using the methods of Gilbert and Cameron (1965), yielding, at 2.5 MeV, 60 keV for J = 1/2, 40 keV for J = 3/2, and 35 keV for J = 5/2. Average level spacings observed in this experiment were: 55 keV for J = 1/2,

140 keV for J = 3/2, and 26 keV for J = 5/2. Only three $\ell = 0$ resonances were observed. All of the data shown have been analyzed, and resonance parameters for the 46 levels are given in table 1.

B. $^{56}Fe(p,p)$

Figure 9 shows the $^{56}Fe(p,p)$ data observed at 160°, with a line to guide the eye. The density of levels is clearly higher than in the $^{54}Fe(p,p)$ data, due to the larger excitation energy (8 - 9 MeV) and the greater neutron excess. These data were analyzed from 2.0 MeV to 3.16 MeV and the resonance parameters were extracted for 99 levels. The predicted level spacing for J = 1/2 is about equal to the observed value, while the observed spacing for J = 5/2 is nearly twenty times as large as the predicted value. This suggests that most of the J = 1/2 levels are observed in this experiment, while many J = 5/2 levels are too narrow to be observed.

The relationship between the levels of the ^{57}Fe - ^{57}Co isobaric pair is shown in fig. 10. The three analogs of the 1.265, 1.627, and 1.725 MeV levels in ^{57}Fe were within the available proton energy range and had widths large enough to be observable in this experiment. Small penetrabilities

precluded observation of the lower-lying levels. The energies of the analog states, E_p^{lab}, were taken from this experiment. Spectroscopic factors for ^{57}Fe states were obtained from the $^{56}Fe(d,p)$ work of Cohen, et al. (1962).

C. $^{58}Fe(p,p)$

Figure 11 shows the relationship between energy levels in the ^{59}Fe - ^{59}Co isobaric pair. The ground state, first excited state and fifth excited state were observed in this experiment. Spectroscopic factors are from the $^{58}Fe(d,p)$ work of Klema, Lee, and Schiffer (1967).

The excitation function for $^{58}Fe(p,p)$ at 160^{o} is displayed in fig. 12, and the solid line through the data is again merely a visual aid. Most of these data were taken using proton energy steps of 100 eV, and the energy scale of fig. 12 does not do justice to some of the small, closely-spaced resonances. The excitation energy in the compound nucleus is 9.4 - 10.5 MeV. Just above 2.2 MeV, the ground state analog appears very strikingly as a cluster of fine structure states. The $1/2^{-}$ analog of the first excited state is also fragmented and appears between 2.50 and 2.55 MeV.

Analysis of these data have been completed from 2.0 to 2.65 MeV, yielding parameters for sixty resonances. The complicated region immediately below 3.0 MeV is associated with the analog of the fifth excited state of ^{59}Fe, but these data are too complex to analyze in detail. An attempt was made to simulate a low resolution experiment by averaging these data with a Gaussian resolution function of ~5 keV width, but the presence of a strong $\ell = 0$ resonance in the middle of the analog region made analysis of the averaged data difficult.

Level spacings were calculated to be 1 keV for J = 1/2 and about 0.5 keV for J = 3/2 or 5/2. In the region of data which was analyzed, many of the levels are clearly not observed. For example, the most favorable case is the 140 keV wide region which includes the $1/2^-$ analog of the first excited state of ^{59}Fe. This region contains ten $1/2^-$ levels and eleven $1/2^+$ levels, yielding an average spacing of nearly 7 keV for J = 1/2. If the Gilbert and Cameron formula is correct, one may conclude that few of the spin 1/2 levels are actually observed. The data above 2.7 MeV show a much greater level density as the higher penetrability increases the observed width of each level.

Figure 7. The ^{55}Fe - ^{55}Co Isobaric Pair. Levels of ^{55}Fe are shifted by the Coulomb energy difference minus the neutron-proton mass difference.

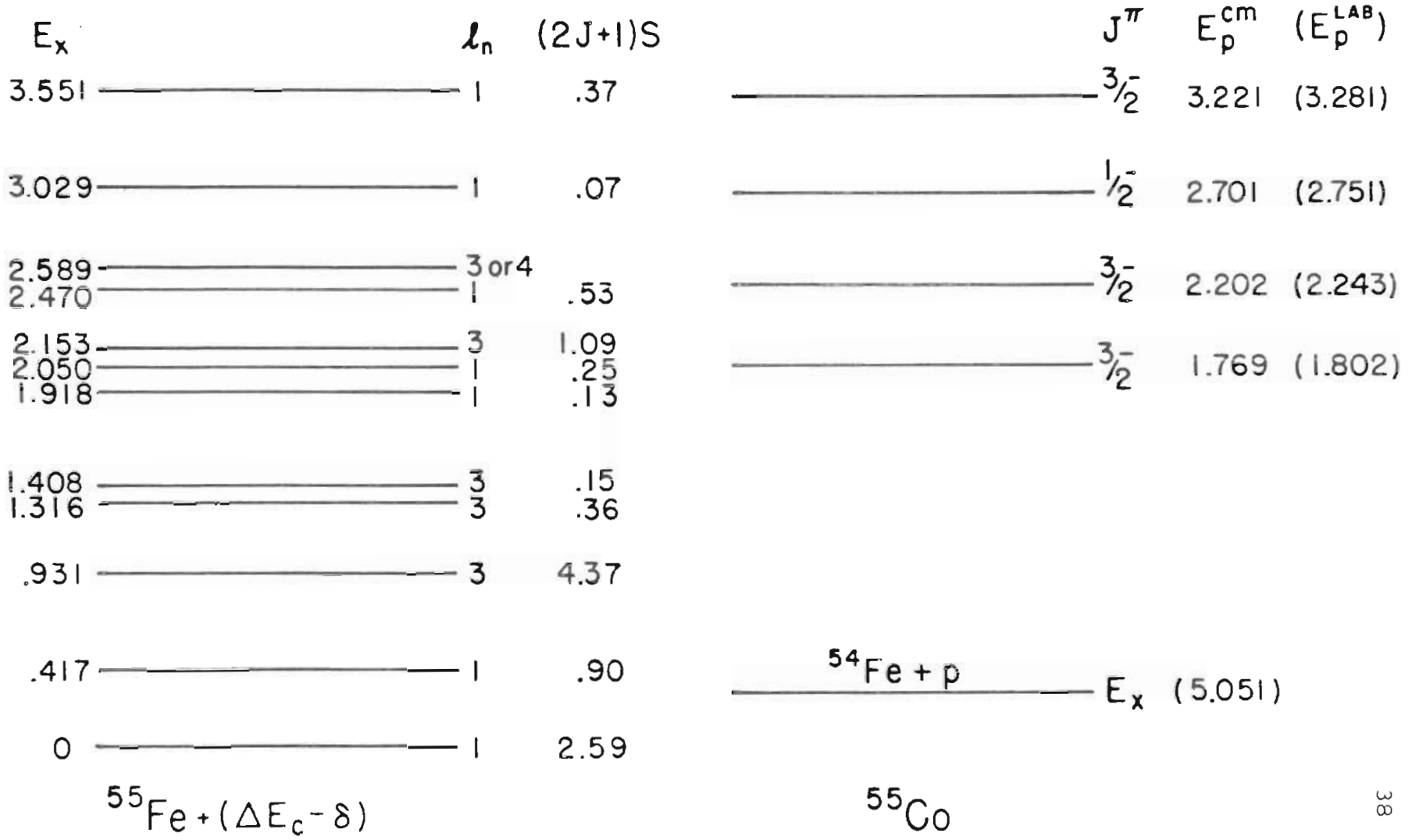
E_x
l_n
(2J+1)S
3.551
1
.37
3.029
1
.07
2.589
3 or 4
2.470
1
.53
2.153
3
1.09
2.050
1
.25
1.918
1
.13
1.408
3
.15
1.316
3
.36
.931
3
4.37
.417
1
.90
0
1
2.59
$^{55}Fe + (\Delta E_c - \delta)$
J^π
E_p^{cm}
(E_p^{LAB})
$3/2^-$
3.221
(3.281)
$1/2^-$
2.701
(2.751)
$3/2^-$
2.202
(2.243)
$3/2^-$
1.769
(1.802)
$^{54}Fe + p$
E_x
(5.051)
^{55}Co

Figure 8. The $^{54}Fe(p,p)$ Differential Cross-section at 160°. The line through the data does not represent a fit.

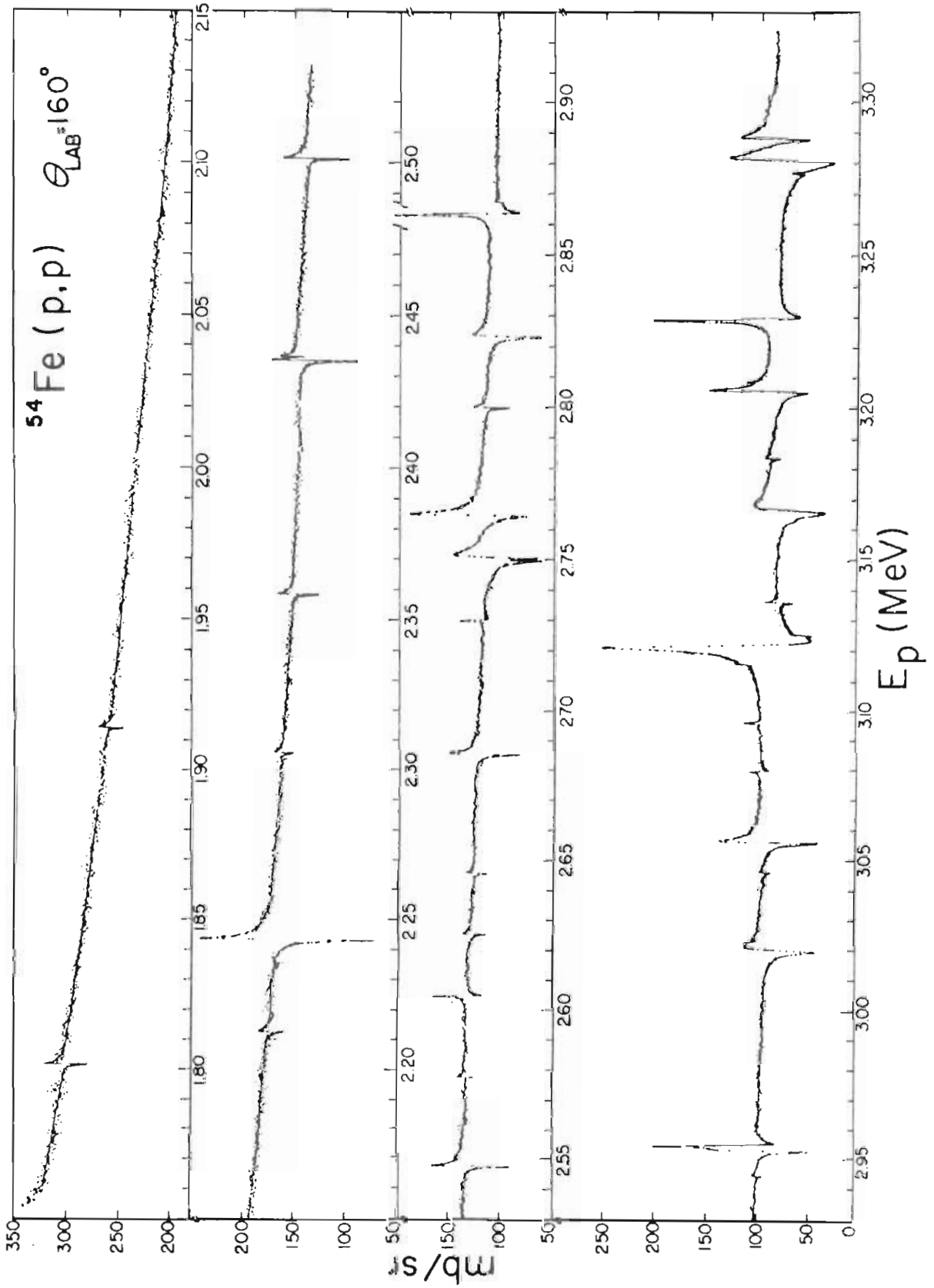
^{54}Fe (p,p) θ_{LAB}=160°
mb/sr
E_p (MeV)

Figure 9. The $^{56}Fe(p,p)$ Differential Cross-section at 160°.

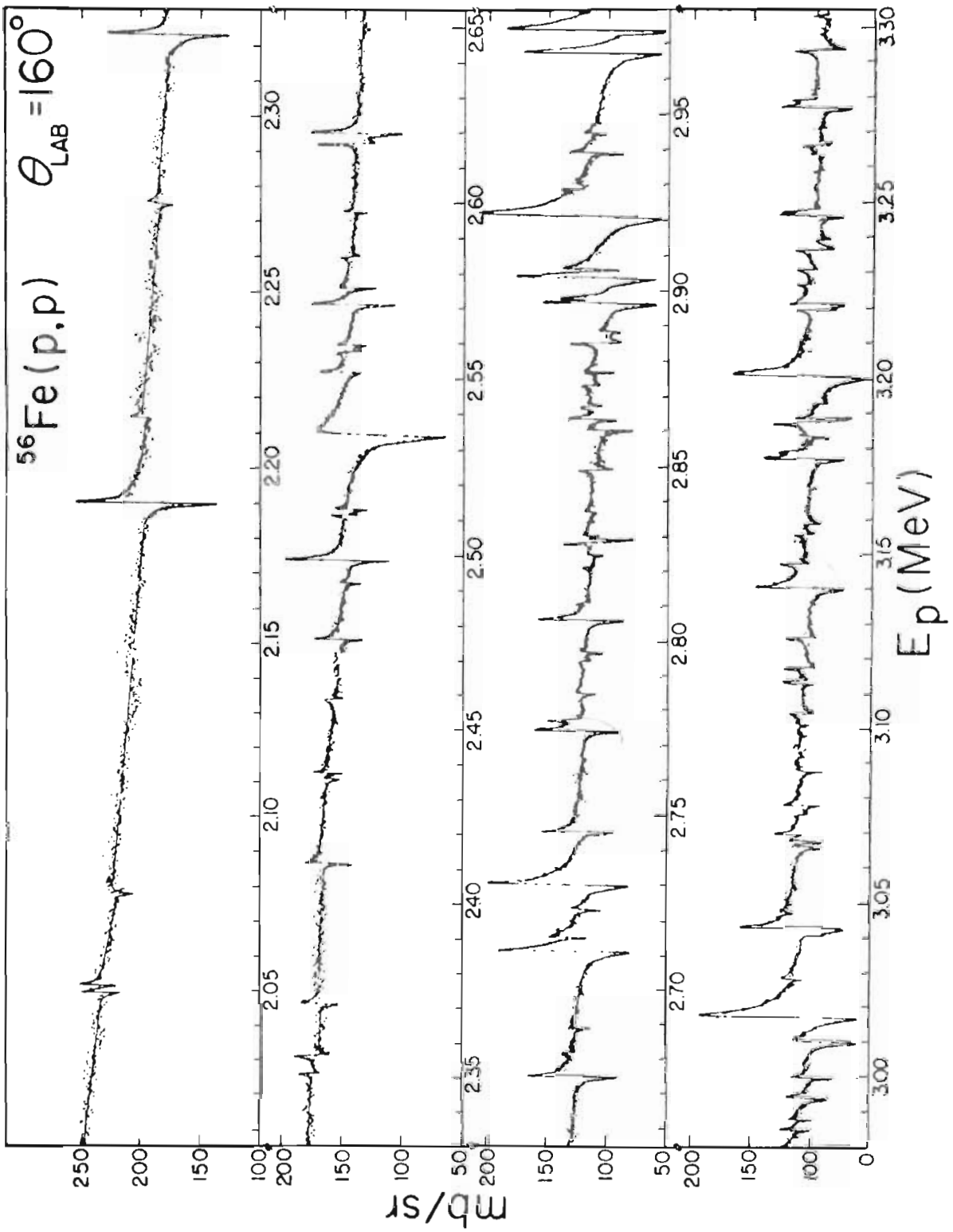
^{56}Fe(p,p) θ_{LAB}=160°
mb/sr
E_p (MeV)

Figure 10. The ^{57}Fe - ^{57}Co Isobaric Pair.

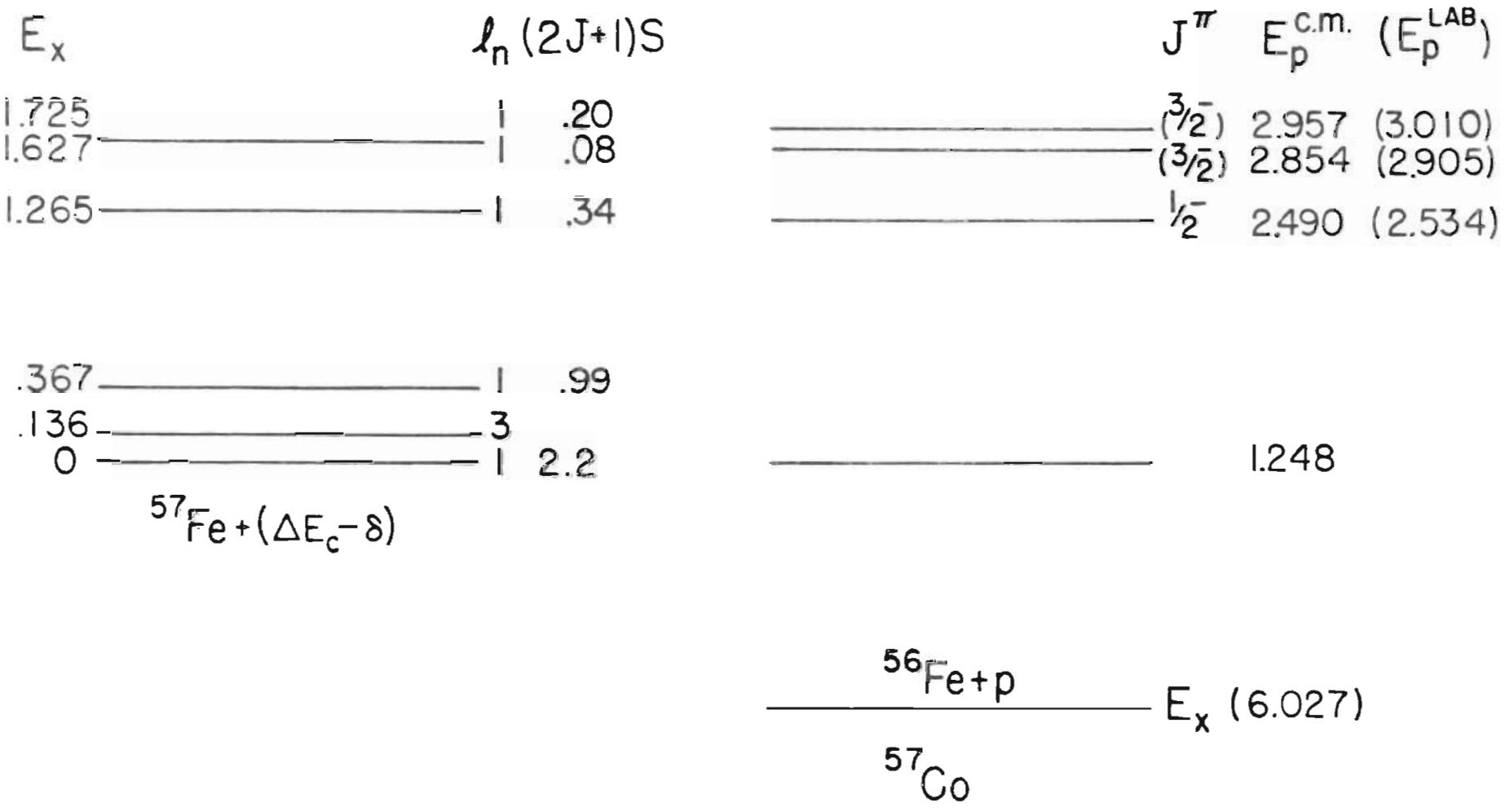
E_x
l_n (2J+1)S
J^π
$E_p^{c.m.}$ (E_p^{LAB})
1.725 1 .20
1.627 1 .08
1.265 1 .34
.367 1 .99
.136 3
0 1 2.2
$^{57}Fe + (\Delta E_c - \delta)$
$(3/2^-)$ 2.957 (3.010)
$(3/2^-)$ 2.854 (2.905)
$1/2^-$ 2.490 (2.534)
1.248
$^{56}Fe + p$
E_x (6.027)
^{57}Co

Figure 11. The ^{59}Fe - ^{59}Co Isobaric Pair.

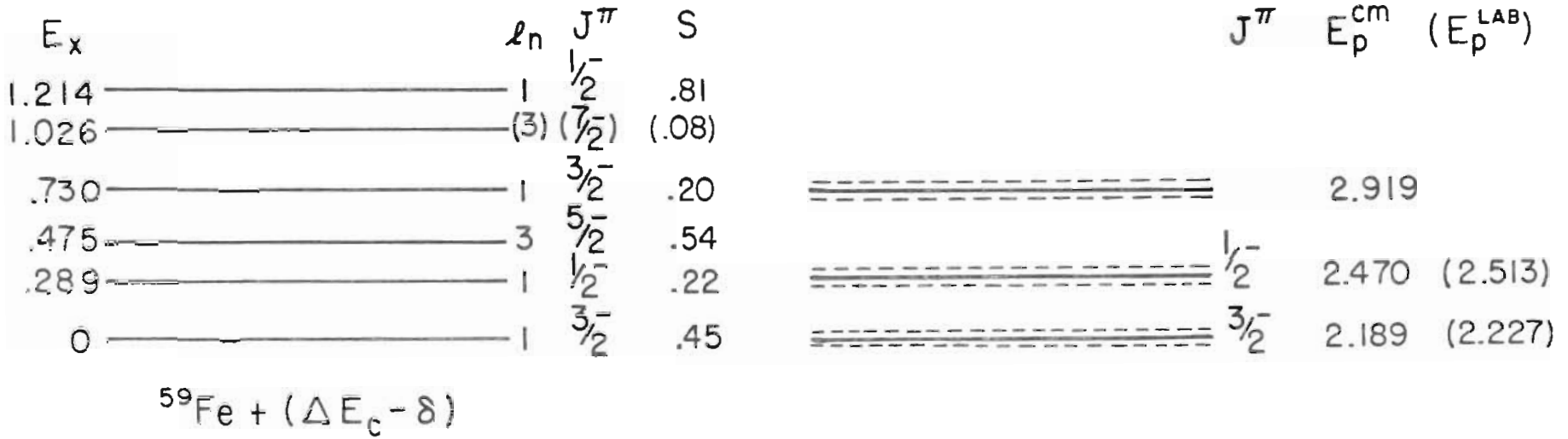
E_x
ℓ_n
J^π
S
1.214
1
1/2-
.81
1.026
(3)
(7/2-)
(.08)
.730
1
3/2-
.20
.475
3
5/2-
.54
.289
1
1/2-
.22
0
1
3/2-
.45
J^π
E_p^{cm}
(E_p^{LAB})
2.919
1/2-
2.470
(2.513)
3/2-
2.189
(2.227)
$^{59}Fe + (\Delta E_c - \delta)$
$^{58}Fe + p$
E_x (7.370)
^{59}Co

Figure 12. The $^{58}Fe(p,p)$ Differential Cross-section at 160^{o}.

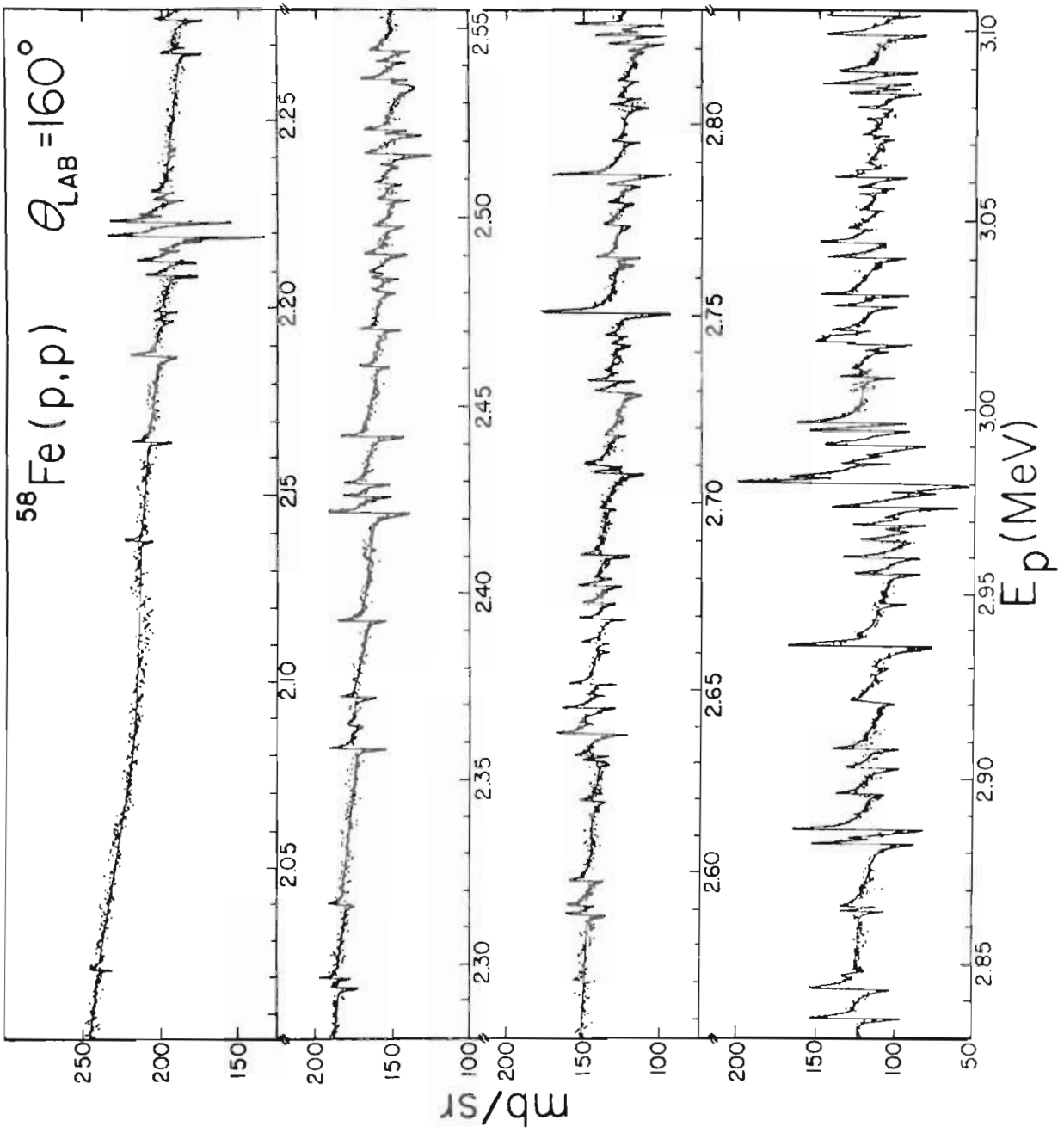
^{58}Fe (p,p) θ_{LAB}=160°
mb/sr
E_p (MeV)

Table 1. $^{54}Fe(p,p)$ Resonance Parameters

E_o(MeV)	J^π	Γ_p(eV)	γ_p^2(keV)
1.8017	(3/2-)	15 ± 8	7.55
1.9141	(1/2-)	20 ± 10	5.89
2.2125	(1/2-)	30 ± 10	2.66
2.2353	(1/2-)	8 ± 5	0.65
2.2431	3/2-	225 ± 40	17.69
2.3055	1/2-	25 ± 10	1.61
2.3584	1/2-	60 ± 15	3.26
2.4352	1/2-	200 ± 25	8.47
2.4363	1/2-	40 ± 10	1.69
2.5012	1/2-	125 ± 20	4.41
2.5474	1/2-	180 ± 30	5.57
2.5776	(3/2-)	20 ± 10	0.57
2.6048	5/2+	35 ± 10	4.07
2.6253	1/2-	35 ± 10	0.88
2.6456	(1/2-)	25 ± 10	0.59
2.6854	1/2-	175 ± 25	3.76
2.7302	(5/2+)	25 ± 10	2.04
2.7500	3/2-	100 ± 20	1.82
2.7509	1/2-	650 ± 60	11.78
2.7647	1/2+	450 ± 50	3.77
2.7997	1/2-	75 ± 15	1.22

Table 1. (continued)

E_o(MeV)	J^π	Γ_p(eV)	γ_p^2(keV)
2.8232	1/2-	350 ± 50	5.39
2.8632	5/2+	180 ± 25	10.32
2.8671	(3/2-)	10 ± 8	0.14
2.9445	1/2+	10 ± 8	0.06
2.9529	1/2-	750 ± 75	8.62
2.9549	5/2+	200 ± 30	9.17
3.0200	1/2-	500 ± 60	5.00
3.0204	1/2-	200 ± 30	2.00
3.0462	1/2-	35 ± 10	0.33
3.0563	3/2-	250 ± 30	2.33
3.0567	3/2-	100 ± 20	0.93
3.0802	(3/2+)	30 ± 10	1.03
3.0963	(5/2-)	8 ± 10	1.87
3.1160	(1/2-)	25 ± 10	0.11
3.1219	5/2+	1200 ± 100	37.64
3.1256	1/2-	60 ± 15	0.49
3.1364	1/2-	70 ± 15	0.56
3.1663	1/2-	1600 ± 120	12.13
3.1835	1/2-	40 ± 15	0.29
3.2057	1/2+	550 ± 60	2.00
3.2090	(3/2+)	15 ± 8	0.39

Table 1. (continued)

E_o(MeV)	J^π	Γ_p(eV)	γ_p^2(keV)
3.2292	5/2+	280 ± 35	7.01
3.2770	3/2-	50 ± 15	0.31
3.2814	3/2-	1400 ± 150	8.61
3.2883	1/2-	500 ± 50	3.04

Table 2. $^{56}Fe(p,p)$ Resonance Parameters

E_o(MeV)	J^π	Γ_p(eV)	γ_p^2(keV)
2.0494	1/2+	30 ± 10	1.96
2.0515	1/2+	30 ± 10	1.94
2.0776	(1/2-)	20 ± 10	2.78
2.1897	1/2+	180 ± 20	7.17
2.3227	1/2+	160 ± 20	4.12
2.3562	(3/2+)	30 ± 10	7.18
2.3510	(3/2+)	20 ± 10	4.87
2.3712	1/2+	35 ± 10	0.78
2.4111	1/2-	50 ± 15	2.18
2.4357	(1/2-)	12 ± 5	0.48
2.4375	1/2+	20 ± 10	0.36
2.4586	(3/2+)	17 ± 10	2.89
2.4759	1/2+	30 ± 10	0.49
2.4920	(1/2-)	20 ± 10	0.68
2.4987	1/2+	140 ± 20	2.17
2.5115	3/2+	30 ± 10	4.29
2.5131	1/2-	40 ± 10	1.27
2.5340	1/2-	1350 ± 120	41.00
2.5519	1/2+	50 ± 10	0.66
2.5573	(3/2+)	15 ± 10	1.86
2.5578	(5/2+)	20 ± 10	2.48

Table 2. (continued)

E_o(MeV)	J^π	Γ_p(eV)	γ_p^2(keV)
2.5597	(3/2-)	25 ± 10	0.70
2.5713	1/2+	85 ± 15	1.07
2.5760	1/2-	40 ± 10	1.07
2.5976	(1/2-)	20 ± 10	0.51
2.6172	5/2+	40 ± 10	4.16
2.6202	1/2+	125 ± 20	1.40
2.6747	1/2+	160 ± 25	1.57
2.6765	(1/2-)	20 ± 10	0.41
2.6814	(3/2+)	12 ± 8	1.04
2.6883	1/2-	30 ± 10	0.60
2.7107	1/2+	500 ± 40	4.52
2.7146	1/2-	60 ± 15	1.12
2.7169	(5/2+)	8 ± 5	0.63
2.7224	(1/2-)	15 ± 10	0.28
2.7299	1/2+	600 ± 50	5.19
2.7446	1/2+	120 ± 20	1.00
2.7738	1/2+	140 ± 15	1.10
2.7746	(3/2+)	15 ± 10	1.01
2.7769	5/2+	35 ± 10	2.34
2.7783	(3/2+)	10 ± 5	0.67
2.7844	(1/2-)	20 ± 10	0.32

Table 2. (continued)

E_o(MeV)	J^π	Γ_p(eV)	γ_p^2(keV)
2.8059	1/2+	140 ± 20	1.02
2.8071	(3/2+)	15 ± 10	0.93
2.8105	(3/2+)	15 ± 10	0.92
2.8210	(3/2+)	10 ± 8	0.60
2.8244	1/2-	30 ± 10	0.43
2.8279	5/2+	40 ± 10	2.34
2.8290	1/2-	120 ± 20	1.71
2.8299	(1/2-)	25 ± 10	0.36
2.8486	3/2+	40 ± 10	2.22
2.8508	(3/2+)	15 ± 8	0.83
2.8553	(3/2+)	10 ± 5	0.54
2.8572	(1/2-)	10 ± 10	0.13
2.8591	(1/2-)	15 ± 10	0.20
2.8600	(1/2-)	85 ± 10	1.13
2.8630	1/2+	60 ± 15	0.39
2.8665	(3/2+)	10 ± 8	0.53
2.8725	(3/2+)	20 ± 10	1.04
2.8760	3/2+	30 ± 10	1.55
2.8763	1/2-	50 ± 15	0.64
2.8845	3/2+	60 ± 15	3.01
2.8878	(1/2-)	25 ± 10	0.31

Table 2. (continued)

E_o(MeV)	J^π	Γ_p(eV)	γ_p^2(keV)
2.8961	1/2+	200 ± 25	1.20
2.8970	1/2+	50 ± 10	0.30
2.9032	1/2+	400 ± 40	2.37
2.9054	(3/2-)	75 ± 20	0.89
2.9209	1/2+	1200 ± 100	6.87
2.9283	(3/2+)	20 ± 10	0.90
2.9297	(1/2-)	15 ± 10	0.17
2.9388	1/2-	90 ± 15	1.00
2.9674	1/2+	450 ± 60	2.35
2.9724	3/2+	40 ± 10	1.63
2.9739	1/2+	850 ± 80	4.39
2.9791	(3/2-)	15 ± 10	0.15
2.9846	1/2+	35 ± 10	0.18
2.9876	1/2-	30 ± 10	0.30
2.9933	1/2+	40 ± 10	0.20
2.9939	1/2+	60 ± 15	0.30
2.9997	1/2-	100 ± 20	0.98
3.0098	3/2-	250 ± 50	2.42
3.0120	(1/2-)	20 ± 10	0.19
3.0173	1/2+	1500 ± 130	7.15
3.0656	1/2-	60 ± 15	0.52

Table 2. (continued)

E_o (MeV)	J^π	Γ_p (keV)	γ_p^2 (keV)
3.0673	1/2-	70 ± 15	0.60
3.0697	1/2+	40 ± 10	0.17
3.0750	(3/2+)	10 ± 8	0.32
3.0781	1/2+	50 ± 10	0.22
3.1042	(3/2+)	15 ± 8	0.46
3.1130	1/2+	30 ± 10	0.12
3.1140	(3/2+)	30 ± 10	0.89
3.1175	3/2+	40 ± 10	0.12
3.1227	3/2+	35 ± 10	1.01
3.1404	1/2+	250 ± 50	0.97
3.1474	(5/2+)	15 ± 10	0.42
3.1490	(3/2+)	10 ± 5	0.28
3.1537	(5/2+)	10 ± 5	0.27
3.1556	(5/2+)	10 ± 5	0.27
3.1576	(3/2+)	15 ± 8	0.41

Table 3. $^{58}Fe(p,p)$ Resonance Parameters

E_o(MeV)	J^π	Γ_p(eV)	γ_p^2(keV)
2.1378	(3/2-)	10 ± 10	1.02
2.1642	1/2+	30 ± 10	1.23
2.1871	(3/2-)	30 ± 10	2.57
2.1966	1/2+	15 ± 10	0.54
2.1990	1/2+	15 ± 10	0.53
2.2085	(3/2-)	30 ± 10	2.34
2.2121	(3/2-)	25 ± 10	1.93
2.2126	1/2+	25 ± 10	0.85
2.2152	(3/2-)	10 ± 8	0.76
2.2178	(3/2-)	15 ± 10	1.13
2.2188	3/2-	95 ± 20	7.16
2.2228	3/2-	80 ± 20	5.94
2.2243	(3/2-)	10 ± 8	0.74
2.2284	(3/2-)	15 ± 10	1.09
2.2304	(3/2-)	10 ± 8	0.72
2.2671	(3/2-)	20 ± 10	1.28
2.2688	(3/2-)	10 ± 8	0.63
2.2764	1/2+	25 ± 10	0.69
2.2931	(3/2-)	10 ± 8	0.59
2.2956	1/2+	15 ± 8	0.39
2.3158	1/2+	25 ± 10	0.62

Table 3. (continued)

E_o(MeV)	J^π	Γ_p(eV)	γ_p^2(keV)
2.3579	1/2+	40 ± 10	0.88
2.3716	1/2+	20 ± 10	0.42
2.3924	1/2+	35 ± 10	0.69
2.4214	1/2+	80 ± 20	1.43
2.4257	1/2+	35 ± 10	0.62
2.4290	1/2+	40 ± 10	0.70
2.4293	(1/2-)	10 ± 8	0.38
2.4417	1/2+	50 ± 15	0.85
2.4602	1/2+	25 ± 10	0.41
2.4702	1/2+	30 ± 10	0.47
2.4799	(1/2-)	25 ± 10	0.82
2.4837	(1/2-)	20 ± 10	0.65
2.4850	(1/2-)	15 ± 10	0.49
2.4901	1/2+	30 ± 10	0.44
2.4975	1/2+	20 ± 10	0.29
2.5041	1/2+	25 ± 10	0.36
2.5083	(1/2-)	15 ± 10	0.45
2.5160	1/2+	50 ± 10	0.69
2.5163	1/2-	50 ± 20	1.48
2.5212	(1/2-)	25 ± 10	0.73
2.5224	1/2+	35 ± 10	0.47

Table 3. (continued)

E_o(MeV)	J^π	Γ_p(eV)	γ^2_p(keV)
2.5254	(1/2-)	15 ± 10	0.43
2.5343	(1/2-)	25 ± 10	0.70
2.5359	1/2+	35 ± 10	0.46
2.5403	(3/2-)	15 ± 10	0.42
2.5435	1/2+	25 ± 10	0.32
2.5706	(1/2-)	25 ± 10	0.64
2.5888	1/2+	40 ± 10	0.46
2.5913	1/2+	25 ± 10	0.28
2.5978	1/2+	30 ± 10	0.34
2.6193	1/2+	20 ± 10	0.21
2.6286	(3/2+)	15 ± 10	1.40
2.6305	1/2+	10 ± 8	0.10
2.6315	1/2+	20 ± 10	0.21
2.6376	1/2+	70 ± 20	0.71
2.6404	(1/2-)	10 ± 8	0.21
2.6446	1/2+	40 ± 10	0.40
2.6480	(3/2-)	10 ± 8	0.21
2.6511	1/2+	45 ± 10	0.44

Chapter V

DISCUSSION

A. Identification of Analog States

The energy of the analog state in the (p + C) system can be estimated by using eq. (3). Excitation energies in the (n + C) system are found from (d,p) experiments. Also, the ℓ-values and spectroscopic factors from (d,p) experiments allow estimates of the expected widths of the analogs, using the relation

$$\Gamma_p = S_{dp}\,\Gamma_{sp}\,/(2T_o + 1). \qquad (7)$$

As described below, plots of reduced widths of each spin are quite useful in identifying analog states.

1. ^{54}Fe(p,p)

Figure 13 displays the cumulative sum of reduced widths for each spin and parity. Since the presence of an analog state enhances the widths of the normal $T_<$ states,

Figure 13. Cumulative Sum of Reduced Widths in $^{54}Fe(p,p)$. The $3/2^-$ analog resonances appear at 1.802, 2.243, and 3.281 MeV. The $1/2^-$ analog is at 2.751 MeV.

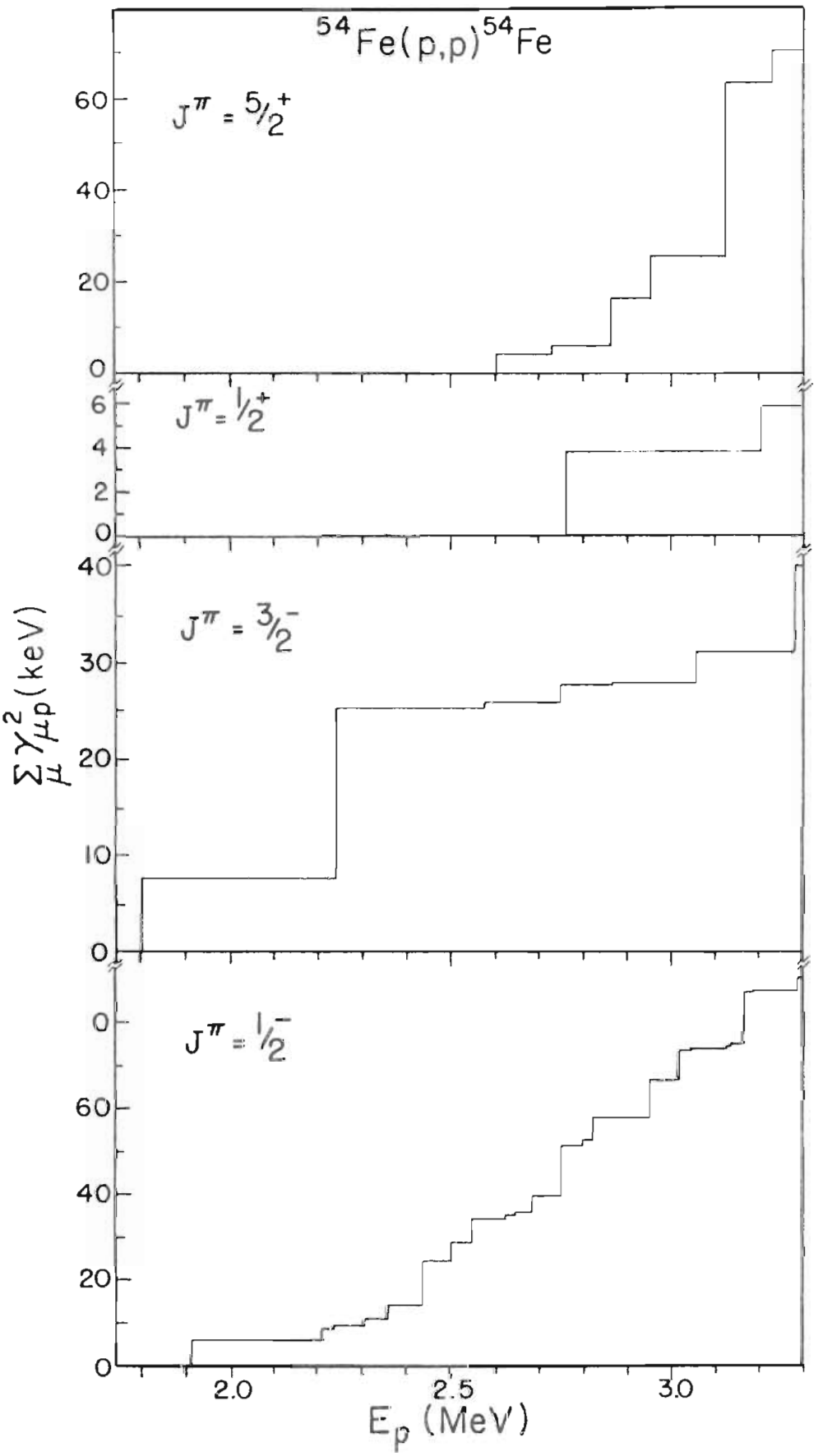
$^{54}Fe(p,p)^{54}Fe$
$J^\pi = 5/2^+$
$J^\pi = 1/2^+$
$J^\pi = 3/2^-$
$J^\pi = 1/2^-$
$\sum_\mu \gamma^2_{\mu p}$ (keV)
E_p (MeV)
0
20
40
60
2
4
6
10
30
2.0
2.5
3.0

a break in the cumulative sum plot is characteristic of an analog. In the plot for $J^{\pi} = 3/2^-$, three analog states are evident at 1.802, 2.243, and 3.281 MeV. Each of these analogs appears as a single strong level except the 3.281 MeV analog, which has two fragments. The spacing between observed resonances is large and appears to be unaffected by the presence of the analogs, suggesting that essentially all $3/2^-$ levels are resolved in this experiment.

The plot for $J^{\pi} = 1/2^-$ is very different from that for $J^{\pi} = 3/2^-$. One analog is identified at 2.751 MeV, but the break in the cumulative sum of reduced widths is not so apparent, due to the very large strength of the T< states. The Coulomb energy difference calculated for this state is consistent with those of the $3/2^-$ analogs, suggesting that the identification of this state as an analog is correct. Again, only a single resonance is believed to constitute the analog, since the level spacing is relatively large.

2. ^{56}Fe(p,p)

In the $1/2^-$ reduced width plot of fig. 14, the analog at 2.534 meV is quite evident. However there are two other analogs in this energy range which do not appear so clearly.

Figure 14. Cumulative Sum of Reduced Widths in $^{56}Fe(p,p)$. The $1/2^-$ analog resonance appears at 2.534 MeV. The $3/2^-$ analogs appear at 2.905 and 3.010 MeV.

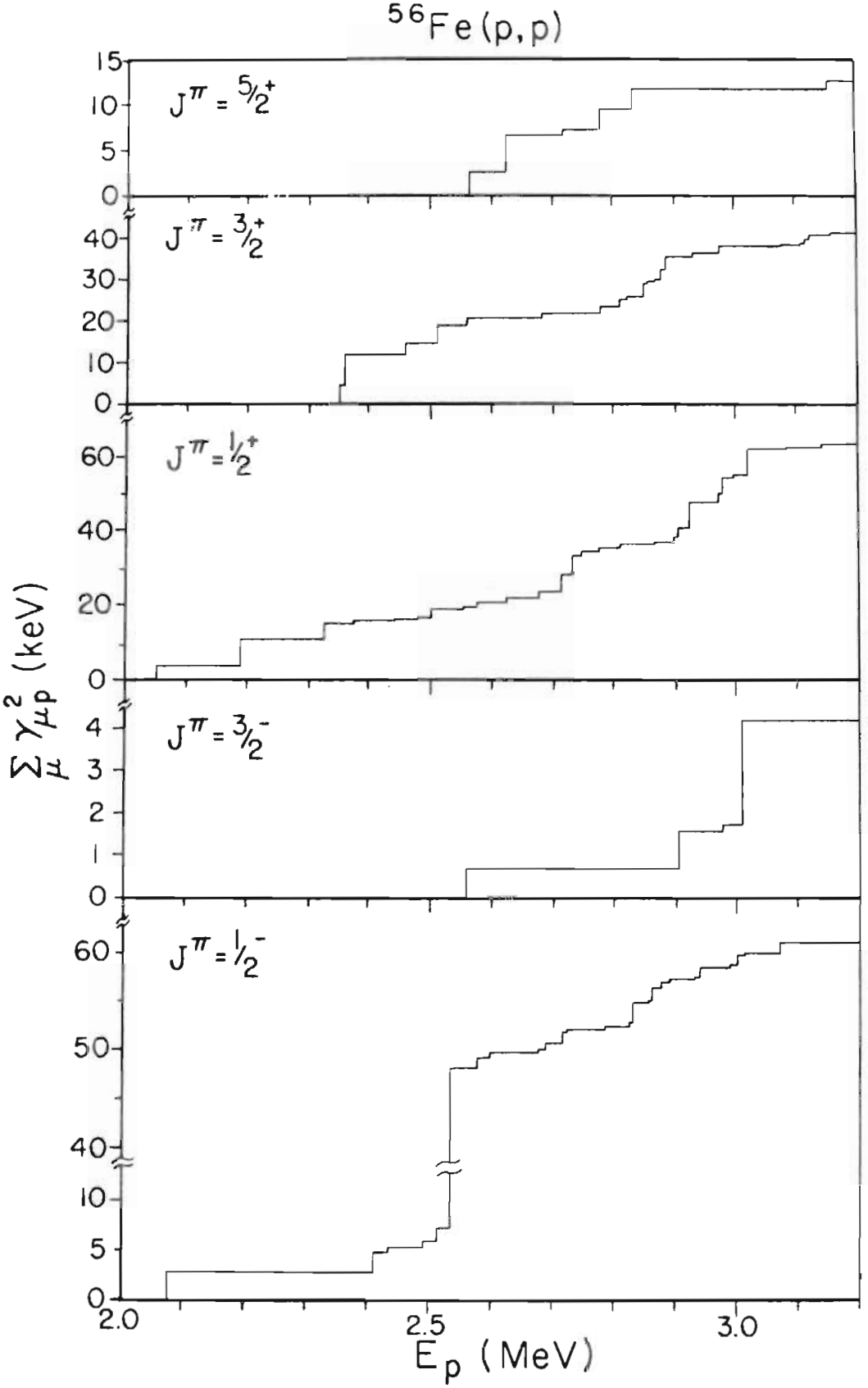
^{56}Fe(p,p)
$J^\pi = 5/2^+$
$J^\pi = 3/2^+$
$J^\pi = 1/2^+$
$J^\pi = 3/2^-$
$J^\pi = 1/2^-$
$\sum_\mu \gamma^2_{\mu p}$ (keV)
E_p (MeV)
2.0
2.5
3.0

since their spectroscopic factors are much smaller. Two $\ell = 1$ analogs should appear at 2.90 and 3.00 MeV. Careful examination of these energy regions does reveal levels at 2.905 and 3.010 MeV which may be identified as analogs.

Analysis of the $^{56}Fe(p,p)$ data yielded a good fit to the suspected analog at 2.905 MeV with $J^{\pi} = 1/2^{-}$, but the $^{56}Fe(p,p'\gamma)$ work of Kyker, et al. (1969) revealed a very strong inelastic peak at this energy, and Kyker's gamma ray angular distribution measurements ruled out $J = 1/2$. This apparent disagreement was resolved when it was found that the elastic data could indeed be fitted with $J^{\pi} = 3/2^{-}$ if an inelastic contribution was included. This led to a careful analysis of the suspected analog at 3.010 MeV, where inelastic proton data had been taken at four angles in the present experiment. In this case, the inelastic and elastic data were fitted simultaneously and again the results indicated a $3/2^{-}$ spin assignment, with a large inelastic width ($\Gamma_{p'} = 300$ ev). In spite of the relatively large $\Gamma_{p'}$ for these two analogs, the inelastic proton yield at the strong 2.534 MeV analog was found to be very small. A further check of inelastic proton yields under $\ell = 0$ and $\ell = 1$ $T_<$ states led to the conclusion that the fits to these data were not appreciably altered by ignoring the partial width for inelastic scattering.

Penetrabilities for inelastic protons are more favorable in the case of $\ell = 2$ resonances, however, and if $\Gamma_{p'}/\Gamma$ is appreciable, the distinction between the characteristic shapes of $3/2^+$ and $5/2^+$ resonances is obscured, even for rather strong levels. The resolution of these problems would require $^{56}Fe(p,p')$ data covering a larger proton energy range and with better statistics and lower background than the limited amount of inelastic data obtained in this experiment.

3. $^{58}Fe(p,p)$

Analogs of the $3/2^-$ ground state and $1/2^-$ first excited state of ^{59}Fe appear in the reduced width plots of fig. 15. The ground state analog is a cluster of fourteen resonances whose centroid is at 2.227 MeV. The centroid of a distribution of levels is defined as

$$\bar{E} = \frac{\sum_i \gamma_i^2 E_i}{\sum_i \gamma_i^2} \qquad (8)$$

The second moment of a distribution of fine structure states is

$$\sigma^2 = \frac{\sum_i \gamma_i^2 (E_i - \bar{E})^2}{\sum_i \gamma_i^2} \qquad (9)$$

This quantity provides a rough indication of the spreading of the analog state. For a normal distribution, the full width at half maximum is

$$\text{FWHM} = (2 \ln 2)^{\frac{1}{2}} \sigma , \tag{10}$$

yielding a value of 75 keV for the ground state analog. The third moment of the distribution,

$$\frac{\sum_i \gamma_i^2 \left(E_i - \bar{E}\right)^3}{\sum_i \gamma_i^2} \tag{11}$$

was found to be positive, indicating an asymmetry toward the high energy side of the centroid. This is opposite to the negative asymmetry predicted by current theories.

The $1/2^-$ reduced width plots of fig. 15 show the analog of the first excited state of ^{59}Fe. This analog appears as ten fine structure states, the centroid of which is at 2.513 MeV. The width of this distribution, 85 keV, is slightly larger than that of the ground state analog. In this instance, the third moment is negative, in agreement with theory. In the center-of-mass system, the energy separation of the two analog states is 0.281 MeV, compared with 0.289 MeV for the separation of the corresponding parent states.

Figure 15. Reduced Widths for ^{58}Fe(p,p) Resonances. Both the individual reduced widths and the cumulative sums are shown. The centroid of the $3/2^-$ ground state analog is 2.227 MeV, while that of the $1/2^-$ analog of the first excited state is 2.513 MeV.

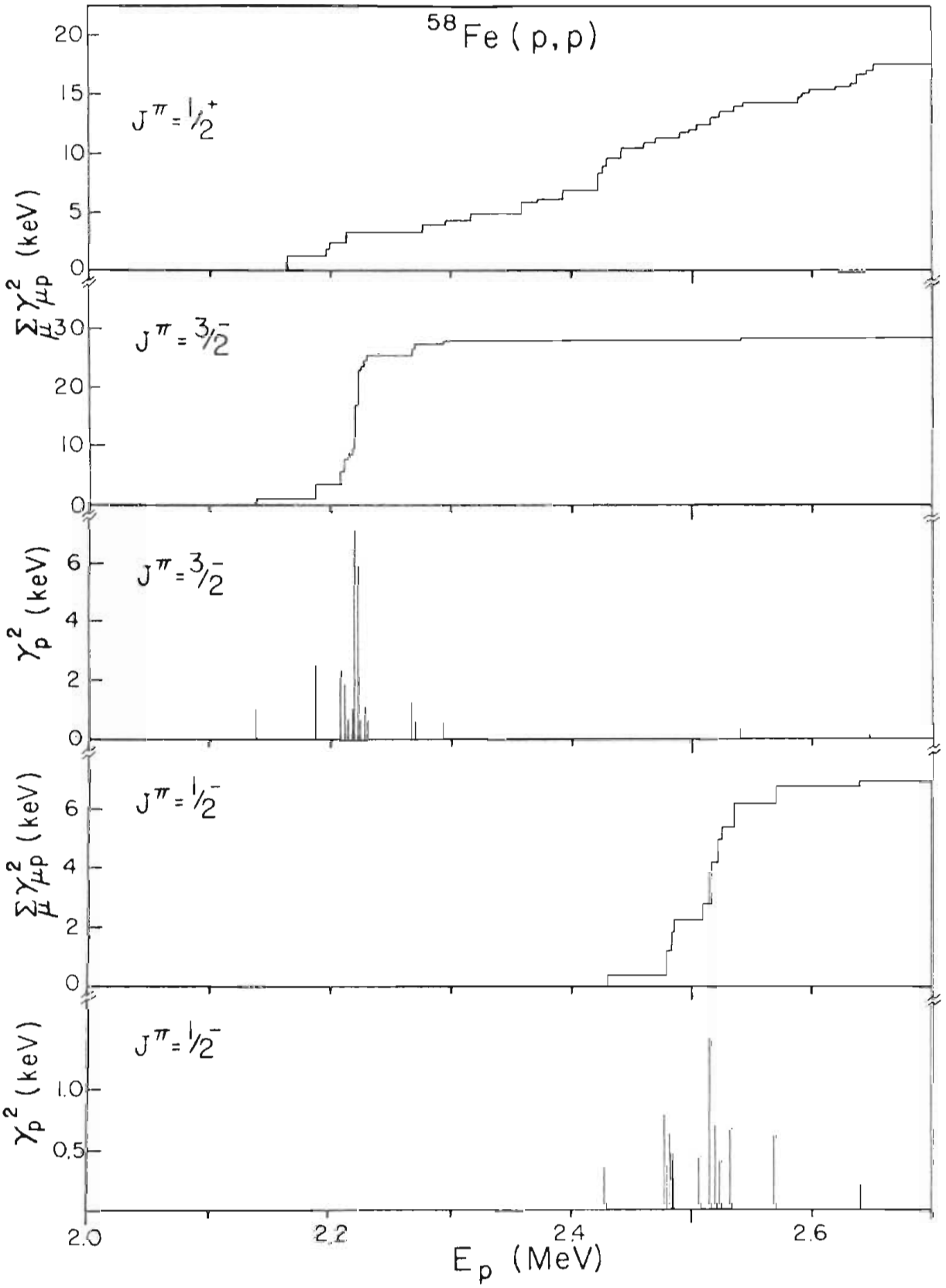
^{58}Fe (p, p)
$J^\pi = 1/2^+$
$\sum_\mu \gamma^2_{\mu p}$ (keV)
$J^\pi = 3/2^-$
$J^\pi = 3/2^-$
γ^2_p (keV)
$J^\pi = 1/2^-$
$\sum_\mu \gamma^2_{\mu p}$ (keV)
$J^\pi = 1/2^-$
γ^2_p (keV)
2.0
2.2
2.4
2.6
E_p (MeV)

B. Spectroscopic Factors

The spectroscopic factor of an analog state can be calculated with the equation

$$S_{pp} = (2T_o + 1)\,\Gamma_p/\Gamma_{sp}, \qquad (12)$$

where T_o is the z-component of the isospin of the target nucleus, Γ_p is the total observed width of the analog state, and Γ_{sp} is the single particle width of the (p + C) state.

This single particle width was calculated using a code written by Harney. This code actually calculates single particle widths using three different, though related methods. A detailed comparison of the assumptions and results of these three methods appears in a paper by Harney and Weidenmüller (1969). The R-matrix method is that of Thompson, Adams, and Robson (TAR), while the other two methods are due to Zaidi, Darmodjo, and Harney (ZDH) and Mekjian and MacDonald (MM).

In calculating single particle widths, the neutron potential was varied to obtain the correct neutron binding energy for the particular state. The corresponding proton well was then calculated by adding to the neutron well a symmetry potential of the form

$$U_{sym} = ((2T_o + 1)/2)(125/A) \text{ MeV}. \qquad (13)$$

The resulting potential was used to calculate the single particle widths shown in table 4. Optical model parameters were from the compilation of Perey, et al. (1968). The dependence of the spectroscopic factor on optical model parameters is discussed by Moses (1970). Agreement between the single particle widths calculated by the methods of ZDH and MM was good, while those of TAR were systematically smaller by 10 - 15%.

Table 5 shows spectroscopic factors calculated from these single particle widths. Spectroscopic factors from (d,p) experiments are also listed, along with the ratio S_{dp}/S_{pp}. For the $3/2^-$ analogs in ^{55}Co this ratio is consistently about 1.5. The $1/2^-$ analog at $E_p^{lab} = 2.751$ yields a spectroscopic factor which is nearly twice as large as S_{dp}. This is puzzling since the level is completely resolved and well isolated from other $1/2^-$ levels.

The spectroscopic factor for the strong analog observed at 2.534 MeV in the ^{56}Fe(p,p) experiment agrees well with (d,p) results. Spectroscopic factors for the other two analogs in ^{57}Co are so small that the poor agreement is not unexpected.

The analogs of the ground state and first excited state of ^{59}Fe are weaker than the (d,p) results would indicate. These analogs are highly fragmented, and the largest

Table 4. Single Particle Widths

Parent	E_p^{lab} (MeV)	J^π	U_n (MeV)	U_p (MeV)	Γ_p (keV)	$\frac{\Gamma_{TAR}}{2T_o+1}$ (keV)	$\frac{\Gamma_{ZDH}}{2T_o+1}$ (keV)	$\frac{\Gamma_{MM}}{2T_o+1}$ (keV)
^{55}Fe	1.802	$3/2^-$	-47.043	-50.515	0.015	0.359	0.404	0.409
	2.243	$3/2^-$	-46.351	-49.823	0.225	2.217	2.426	2.443
	2.751	$1/2^-$	-48.361	-51.833	0.650	8.794	10.32	10.34
	3.281	$3/2^-$	-44.503	-47.975	1.40	26.93	29.07	29.24
^{57}Fe	2.534	$1/2^-$	-47.614	-53.194	1.35	3.899	4.790	4.873
	2.905	$(3/2^-)$	-44.118	-49.698	0.075	10.46	12.41	12.50
	3.010	$(3/2^-)$	-43.956	-49.536	0.250	12.96	15.31	15.43
^{59}Fe	2.227	$3/2^-$	-44.274	-51.817	0.370	1.349	1.616	1.634
	2.513	$1/2^-$	-46.612	-54.155	0.225	3.272	3.962	4.001

$U_p = U_n - ((2T_o+1)/2)\ (125/A)$

$R_1 = 1.287\ A^{1/3}$ fm

$R_3 = 1.274\ A^{1/3}$ fm

$R_c = 1.250\ A^{1/3}$ fm

$A_1 = A_2 = 0.65$ fm

Table 5. Spectroscopic Factors

Isobaric Pair	E_x of Parent (MeV)	E_p^{lab} (MeV)	J^π	S_{TAR}	S_{ZDH}	S_{MM}	$\overline{S}_{pp}$	S_{dp}	Ratio[a]
^{55}Fe - ^{55}Co	2.050	1.802	$3/2^-$	.042	.037	.036	.038	.06	1.6
	2.470	2.243	$3/2^-$	.102	.093	.092	.096	.13	1.4
	3.029	2.751	$1/2^-$	.074	.063	.063	.067	.035	0.52
	3.551	3.281	$3/2^-$	.052	.048	.048	.049	.09	1.9
^{57}Fe - ^{57}Co	1.266	2.534	$1/2^-$	.35	.28	.28	.30	.34	1.1
	1.627	2.905	$(3/2^-)$	.007	.006	.006	.006	.02	3.3
	1.725	3.010	$(3/2^-)$	.019	.016	.016	.017	.05	2.9
^{59}Fe - ^{59}Co	0.0	2.227	$3/2^-$	.27	.23	.23	.24	.45	1.9
	0.287	2.513	$1/2^-$	.069	.057	.056	.061	.22	3.6

a. Ratio = S_{dp}/S_{pp}

fragment observed is only 95 eV wide. It appears that some of the strength of these analogs may be contained in resonances too small to be observed in this experiment (<10 eV). This effect should be partially cancelled by the fact that no correction for the background $T_<$ states was made, but it is impossible to estimate the extent of this cancellation, since few $\ell = 1$ resonances were observed away from analog regions.

C. Coulomb Energy Differences

The Coulomb energy difference between the parent and analog states was calculated using the relation

$$\Delta E_c = B_n + E_p^{CM} - E_x, \qquad (14)$$

where B_n is the binding energy of the last neutron in the (n + C) system and E_x is the excitation of the parent state. The energy of the analog state in the (p + C) system, E_p^{CM}, is taken to be the centroid of the distribution of levels comprising the analog state, in the center-of-mass system. Table 6 shows the results of this calculation for each of the analog states observed in these experiments. The Coulomb energy differences quoted from the literature are the differences between the ground states of the isobaric pair.

Table 6. Coulomb Energy Differences

Isobaric Pair	E_x of Parent (MeV)	E_p^{lab} (MeV)	J^π	ΔE_c (Present Work) (MeV)	ΔE_c (Other Sources) (MeV)	$\frac{\Delta E_c}{(Z/A^{1/3})}$
^{55}Fe - ^{55}Co	2.050	1.802	$3/2^-$	9.018 ± .005	9.033 ± .005[a]	1.319
	2.470	2.243	$3/2^-$	9.031 ± .005		1.321
	3.029	2.751	$1/2^-$	8.979 ± .005		1.313
	3.551	3.281	$3/2^-$	8.970 ± .005		1.312
^{57}Fe - ^{57}Co	1.266	2.534	$1/2^-$	8.871 ± .005	8.939 ± .015[a]	1.313
	1.627	2.905	$(3/2^-)$	8.874 ± .005		1.313
	1.725	3.010	$(3/2^-)$	8.878 ± .005		1.315
^{59}Fe - ^{59}Co	0.0	2.227	$3/2^-$	8.775 ± .010		1.314
	0.289	2.513	$1/2^-$	8.767 ± .012		1.313

a. Jänecke (1969).

The errors quoted in table 6 arise from a number of sources. Errors in the published values of the binding energy of the last neutron (B_n) range from 0.5 keV in ^{57}Co to 4.1 keV in ^{59}Co. The excitation energies of the parent states are typically uncertain by a few kilovolts. Where the analog state is observed as a single level, its energy is known to within the estimated absolute energy calibration of the accelerator ($\pm$ 3 keV). Fragmented analog states introduce an additional uncertainty, since it is often difficult to decide which levels to include when calculating the centroid of the distribution.

Also given in table 6 is the ratio $\Delta E_C/ZA^{-1/3}$, which should be nearly constant to first approximation. An empirical formula based on a systematic analysis of available Coulomb displacement energies (Jänecke, 1969) is

$$\Delta E_C = (1389\ Z_< - 2041)\ A^{-1/3}\ \text{keV}. \qquad (15)$$

For the iron isotopes, this formula yields $\Delta E_C/ZA^{-1/3} = 1.311$. This is in good agreement with the value of 1.314, obtained from a least-squares fit to the values of ΔE_C derived from this experiment.

D. Proton Strength Functions

The strength function is defined as the ratio of the average reduced width of a group of levels to the average spacing of the levels. Data away from analog regions contain information on the proton strength functions for the $T_<$ states. An attempt was made to extract these strength functions by calculating the best straight-line fit to the cumulative sums of the reduced widths for each spin. The slopes of these lines are the strength functions tabulated in table 7. In several instances, only a few levels of a given spin were observed, and no reliable strength function could be calculated. In the $^{58}Fe(p,p)$ experiment, few resonances with $\ell \neq 0$ were seen except near the analogs, so only the $1/2^+$ strength function could be calculated.

The errors in the strength functions are generally quite large due to accumulated errors in the sums or a small statistical sample. Nevertheless, the values given should represent a reasonable lower limit to the actual strength functions.

Table 7. Proton Strength Functions

Target Nucleus	J^{π}	$\left\langle \frac{\gamma_p^2}{D} \right\rangle$	Error	No. of Levels	Ratio*
^{54}Fe	$1/2^-$	.07	$\pm$ .01	11	1.8
	$3/2^-$	.009	$\pm$ .004	5	0.2
	$5/2^+$	.09	$\pm$ .03	6	2.4
^{56}Fe	$1/2^+$	.05	$\pm$ .01	32	1.3
	$1/2^-$	.025	$\pm$ .005	39	0.9
	$3/2^+$	.04	$\pm$ .01	27	1.0
	$5/2^+$	.015	$\pm$ .006	8	0.4
^{58}Fe	$1/2^+$	.033	$\pm$ .005	32	0.9

*Ratio is the proton strength function, $\langle \gamma_p^2/D \rangle$, divided by the equivalent "black nucleus" value (0.038).

Chapter VI

SUMMARY

This experiment is one of a series being carried out in this laboratory to investigate analog states using high resolution proton scattering. It is hoped that some rather general features of statistical aspects such as proton strength functions, distributions of reduced widths, and level spacings will become discernable as more data are collected and analyzed.

At least seven analog states were observed in elastic proton scattering on ^{54}Fe, ^{56}Fe, and ^{58}Fe. Since the level densities in ^{55}Co and ^{57}Co were rather small, there was little mixing of the $T_<$ and $T_>$ states, and the analogs were not highly fragmented. In ^{59}Co, where the density of $T_<$ states was large, the analogs were split into many fine structure states.

Spectroscopic factors which were calculated for the analog states tended to be smaller than those obtained from (d,p) experiments. In one instance, however, the spectroscopic factor was found to be considerably larger than the

corresponding (d,p) value. Coulomb energy differences between parent states and analogs were found to be both internally consistent and consistent with other results.

Analysis of the limited inelastic proton scattering data suggested that a more comprehensive study of these data might be useful. Recent improvements in the target chamber have made this undertaking more feasible by greatly reducing the background under the inelastic peaks.

It is clear that high resolution elastic proton scattering continues to be an extremely useful means of increasing our understanding of the detailed properties of analog states.

APPENDIX

Appendix

DIGITAL DATA READOUT SYSTEM

Previously, excitation functions for high resolution proton scattering had been taken entirely by hand. Energy values and the corresponding number of counts from detectors at various angles were written in data books for later transcription to punched cards. When four or more detectors were used simultaneously and the accumulation time was on the order of 20 sec, the time spent writing numbers in data books and resetting the energy for the next point could easily exceed the actual accumulation time. In addition, a keypunch operator spent many hours punching the thousands of data points gathered in a typical machine run. It was decided to seek a more efficient data handling system, so that data on many isotopes could be taken and analyzed in a reasonable length of time.

Several possibilities were apparent. An on-line computer was available, but the use of a computer as a

multiple scaler would be grossly inefficient, particularly considering the high counting rates observed in these experiments. Since the computer is time-shared with the Triangle Universities Nuclear Laboratory tandem accelerator laboratory and the 4 MV accelerator laboratory, the large dead times which the other computer users would experience would be intolerable. Another objection to any on-line computer system was that data would necessarily be output onto magnetic tape, and it would be difficult to edit the tapes to remove bad data points, replace blocks of data that had been repeated, and find specific regions of data for analysis. These considerations also ruled out the use of an off-line incremental tape drive for storing data. Paper tape is another medium that was considered, but again editing and transcribing onto magnetic tape would be required before analysis could be performed.

Thus it was decided to design a digital data handling system which would read out each data point into a standard keypunch. Such a system would provide printed and punched cards which could easily be edited and portions of data could be selected for analysis at one of several card-reading terminals connected to the IBM 360 computer. The format of data cards would be determined by the drum control card in the keypunch.

Since no commercial equipment meeting this need was available, the author designed and built a data handling system. The system was to be as flexible as possible, so that it would be compatible with a variety of experiments. Preliminary specifications included provisions for eight six-digit data sources, plus a thumbwheel for entering the energy on each card. The IBM 029 keypunch was leased, so connections to it were to be kept to a minimum. A digital printer was included also, partly as a backup in case of a keypunch failure and partly to record data points from one or two scalers so that they could be plotted by the experimenter during the data run.

The data handling system envisioned would have been prohibitively complex if it were built using discrete components, so integrated circuits were used wherever possible. Motorola MDTL integrated circuits were selected because of their low cost, adequate noise immunity, and compatibility with the Texas Instruments TTL circuits which were used for a few of the more complex logical functions. Fifty integrated circuits and sixty discrete transistors were required. The complexity of the electronics is illustrated by the fact that the final design, including integrated circuits, comprised 910 transistors, 1136 diodes, and 1407 resistors.

The various functions of the system were broken down

into logical units which could be constructed on a small number of circuit boards. For each board, the integrated circuits and discrete components required to obtain the proper logical functions were selected, and a tentative wiring diagram was made. Since the circuit boards were to be copper-clad on only one side, an effort was made to minimize the number of jumpers required to interconnect the components. A double-sized drawing of each circuit board was made, using a tape pen to represent conductors and tape circles for terminals. These drawings were photographically reduced to half size and the sensitized 7.6 x 15.3 cm glass-epoxy circuit boards were exposed through the resulting negatives. Fourteen different circuit boards were required.

All circuit boards were designed to plug into 18- or 22-terminal sockets, which required consolidating logical units so that as many interconnections as possible could be made on the circuit boards themselves. The sockets used had wire-wrap terminals, which greatly facilitated the final wiring process. In addition, a 100-pin wire-wrap terminal block was included to handle data lines and other miscellaneous connections.

Provisions were made for eight external data sources in addition to the internal thumbwheel. The scalers to be used with the system had six-digit BCD parallel output, or

twenty-four data lines per scaler. Each of these data lines was connected to a common data bus, and all had to be diode-isolated. The problem of mounting the 192 isolation diodes was solved by mounting them on small circuit boards which were soldered directly to the 50-pin data plugs leading to the scalers.

The data readout system was built in an aluminum frame which was mounted on a sliding relay rack mount, so the chassis could easily be pulled out for testing or repair. An anodized aluminum door on the front panel may be opened to give access to the circuit boards and panel switches. To provide the $\pm$ 5 V and $\pm$ 10 V required, a regulated power supply was built on a separate chassis. The transistors which actually drive the punch interposer magnets were mounted in a separate box near the keypunch in an effort to isolate electrical noise generated by the keypunch.

Basically the data readout system converts parallel data from the scalers, timer, and thumbwheel into serial BCD form, decodes it to decimal form, and drives the keypunch through several buffer amplifiers. The printer requires data in parallel BCD format, so no decoding is necessary for printed output. The remainder of the circuitry enables each device in sequence, starts and stops the readout cycle, provides the proper timing pulses, and generates device

identification numbers to facilitate reading the printer output. A block diagram of the data readout system is shown in fig. 16.

The readout cycle may be started in several ways. In the automatic mode, readout begins when the counting cycle stops at the end of a preset time or when a preset amount of charge or number of counts is accumulated. A button on the front panel may be used to start the readout cycle manually. Pressing another button resets all scalers and the current integrator, and releasing the button starts a new counting cycle.

For each of the nine possible data sources, a pair of miniature switches selects whether that device is to be printed or punched. Also, a row of lamps indicates the status of the readout cycle at any time, providing a visual check on the operation of the system. The Van de Graaff energy is read into the data system with a six-digit thumbwheel. An interlock is provided, so that the scalers cannot be read out until the thumbwheel data has been entered with a button on the front panel. This insures that the energy appears in the proper place on each punched card. Another button aborts the readout cycle by initializing the logic, and also releases the card from the punch station in the keypunch. It is sometimes useful to insert blank cards into

the data by depressing this button one or more times.

Taking data using the digital readout system has proved to be much easier and faster than previously. The thumbwheel is normally set to the proper energy and read out while the data for that energy is being accumulated. When the preset charge has been accumulated, the remainder of the readout cycle begins automatically. The time required to read out four scalers and a digital timer is about three seconds. Meanwhile, the experimenter can set the digital voltmeter and magnet power supply for the next energy point. Since this takes about five seconds, the readout cycle is completed by the time the machine energy is set, and the experimenter presses the "reset" button to begin accumulating the next data point. Thus the amount of machine time wasted is very small.

Figure 16. Block Diagram of Data Readout System.

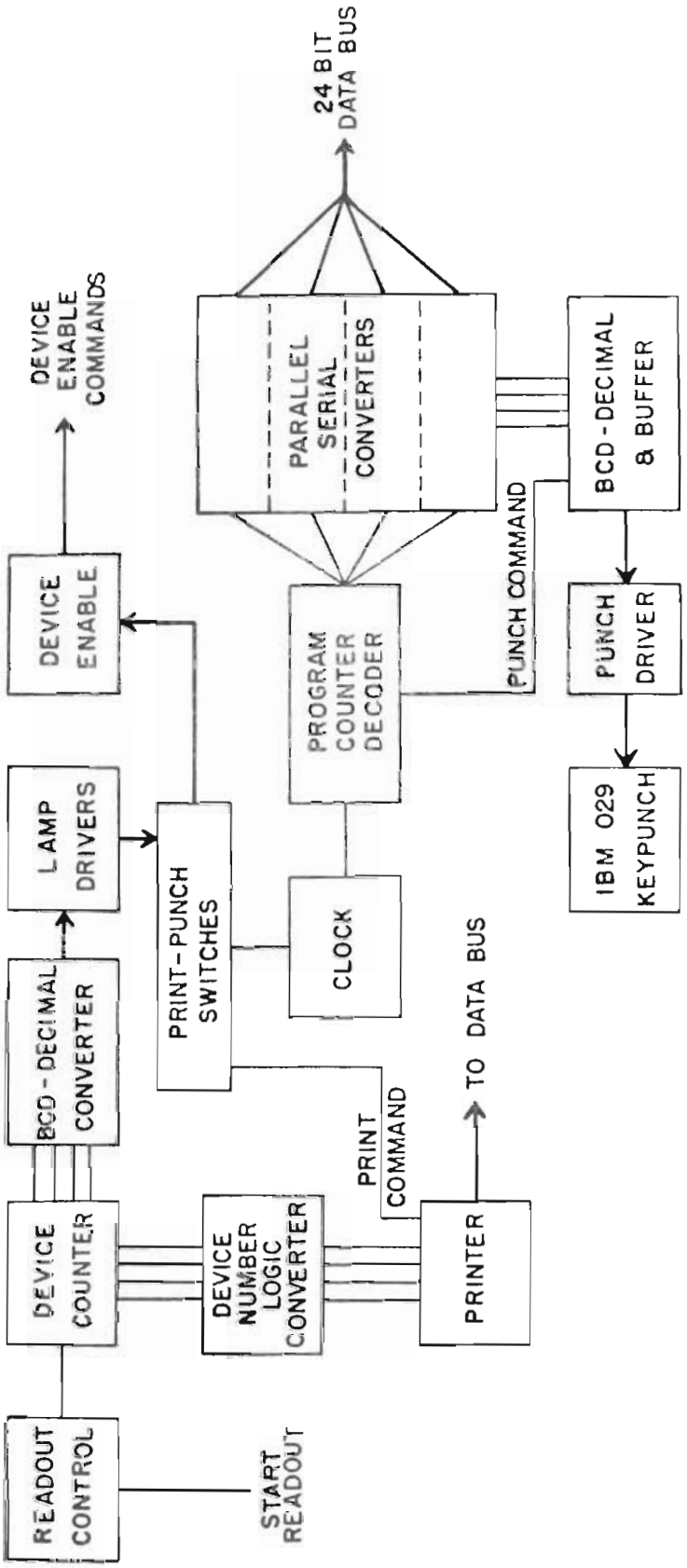
24 BIT DATA BUS
DEVICE ENABLE COMMANDS
PARALLEL SERIAL CONVERTERS
BCD-DECIMAL & BUFFER
DEVICE ENABLE
PROGRAM COUNTER DECODER
PUNCH COMMAND
PUNCH DRIVER
LAMP DRIVERS
PRINT-PUNCH SWITCHES
CLOCK
IBM 029 KEYPUNCH
BCD-DECIMAL CONVERTER
TO DATA BUS
PRINT COMMAND
DEVICE COUNTER
DEVICE NUMBER LOGIC CONVERTER
PRINTER
READOUT CONTROL
START READOUT

LIST OF REFERENCES

LIST OF REFERENCES

J. D. Anderson, C. Wong, and J. W. McClure, Phys. Rev. 126, 2170 (1962).

J. C. Browne, G. A. Keyworth, P. Wilhjelm, D. P. Lindstrom, J. D. Moses, H. W. Newson and E. G. Bilpuch, Physics Letters 28B, 26 (1968).

J. C. Browne, "Fine Structure of Analog States in ^{61}Cu, ^{63}Cu, and ^{65}Cu", unpublished Ph.D. dissertation, Duke University, (1969).

B. L. Cohen, R. H. Fulmer, and A. L. McCarthy, Phys. Rev. 126, 698 (1962).

J. D. Fox, C. F. Moore, and D. Robson, Phys. Rev. Letters, 12, 198 (1964).

R. H. Fulmer and A. L. McCarthy, Phys. Rev. 131, 2133 (1963).

A. Gilbert and A. G. W. Cameron, Canadian Journal of Physics, 43, 1446 (1965).

M. L. Gursky, Los Alamos Scientific Laboratory (unpublished).

H. L. Harney and H. A. Weidenmüller, Nuclear Physics A139, 241 (1969).

J. Jänecke, Isospin in Nuclear Physics, D. H. Wilkinson, ed., North-Holland Publishing Company (1969).

G. A. Keyworth, G. C. Kyker, Jr., E. G. Bilpuch, and H. W. Newson, Nuclear Physics 89, 590 (1966).

G. A. Keyworth, "A High Resolution Study of Isobaric Analogue States in ^{41}K and ^{23}Na", unpublished Ph.D. dissertation, Duke University, (1968).

E. D. Klema, L. L. Lee, Jr., and J. P. Schiffer, Phys. Rev. 161, 1134 (1967).

G. C. Kyker, Jr., E. G. Bilpuch, and H. W. Newson, Annals of Physics 51, 124 (1969).

A. M. Lane and R. G. Thomas, Rev. Mod. Phys. 30, 257 (1958).

A. M. Lane, Nuclear Physics 35, 676 (1962).

J. R. Maxwell and W. C. Parkinson, Phys. Rev. 135, B82 (1964).

J. D. Moses, "A High Resolution Study of Isobaric Analog Resonances in ^{51}Mn, ^{53}Mn, and ^{55}Mn", unpublished Ph.D. Dissertation, Duke University (1970).

P. B. Parks, H. W. Newson, and R. M. Williamson, Rev. Sci. Instr. 29, 834 (1958).

C. M. Perey, F. G. Perey, J. K. Dickens, and R. J. Silva, Phys. Rev. 175, B1460 (1968).

P. Richard, C. F. Moore, J. D. Fox, and D. Robson, Phys. Rev. Letters 13, 343 (1964).

D. Robson, Phys Rev. 137, B535 (1965).

D. Robson, Ann. Rev. Nucl. Sci. 16, 119 (1966).

F. T. Seibel, Jr., "Neutron Resonances in ^{34}S, ^{40}A, and ^{48}Ca", unpublished Ph.D. Dissertation, Duke University (1968).

D. L. Sellin, "Excited States in ^{19}F", unpublished Ph.D. dissertation, Duke University (1968).

E. P. Wigner and L. Eisenbud, Phys. Rev. 72, 29 (1947).

P. Wilhjelm, G. A. Keyworth, J. C. Browne, W. P. Beres, M. Divadeenam, H. W. Newson, and E. G. Bilpuch, Phys. Rev. 177, 1553 (1969).

BIOGRAPHY

Daniel Peter Lindstrom

Personal: Born 28 April 1943, Ashland, Wisconsin

Education: B. S. in Physics, Carleton College, 1965

Positions: Teaching Assistant, Duke University, 1965-66
Research Assistant, Duke University, 1966-present

Memberships: American Physical Society
Sigma Xi

Publications:

1. The Fine Structure of Isobaric Analogue Resonances in ^{43}Sc and ^{45}Sc (with J.C. Browne, G.A. Keyworth, J.D. Moses, P. Wilhjelm, H.W. Newson, and E.G. Bilpuch). Physics Letters 28B, 26 (1968).

2. The Fine Structure of Isobaric Analogs of the Ground and Second Excited States of ^{63}Ni (with J.C. Browne, J.D. Moses, G.E. Mitchell, H.W. Newson, and E.G. Bilpuch). Nuclear Isospin--Proceedings of the Conference on Nuclear Isospin, Asilomar, Calif., Academic Press (1969).

Abstracts:

1. Fine Structure of Isobaric Analog Resonances in ^{55}Co, ^{57}Co, and ^{59}Co (with G.E. Mitchell, H.W. Newson, and E.G. Bilpuch). Bull. Am. Phys. Soc. 14, 1208 (1969).

2. Fine Structure of Isobaric Analog Resonances in ^{63}Cu (with J.C. Browne, J.D. Moses, G.E. Mitchell, H.W. Newson, and E.G. Bilpuch). Bull. Am. Phys. Soc. 14, 589 (1969).